doi.org/10.26434/chemrxiv.11919039.v1

Spin–Phonon Coupling and Dynamic Zero-Field Splitting Contributions to Spin Conversion Processes in Iron(II) Complexes

Nicholas Higdon, Alexandra Barth, Patryk Kozlowski, Ryan Hadt

Submitted date: 01/03/2020 • Posted date: 03/03/2020

Citation information: Higdon, Nicholas; Barth, Alexandra; Kozlowski, Patryk; Hadt, Ryan (2020): Spin–Phonon Coupling and Dynamic Zero-Field Splitting Contributions to Spin Conversion Processes in Iron(II) Complexes. ChemRxiv. Preprint. https://doi.org/10.26434/chemrxiv.11919039.v1

Magnetization dynamics of transition metal complexes manifest in properties and phenomena of fundamental and applied interest (e.g., slow magnetic relaxation in single molecule magnets (SMMs), quantum coherence in quantum bits (qubits), and intersystem crossing (ISC) rates in photophysics). While spin–phonon coupling is recognized as an important determinant of these dynamics, additional fundamental studies are required to unravel the nature of the coupling and thus leverage it in molecular engineering approaches. To this end, we describe here a combined ligand field theory and multireference ab initio model to define spin–phonon coupling terms in S = 2 transition metal complexes and demonstrate how couplings originate from both the static and dynamic properties of ground and excited states. By extending concepts to spin conversion processes, ligand field dynamics manifest in the evolution of the excited state origins of zero-field splitting (ZFS) along specific normal mode potential energy surfaces. Dynamic ZFSs provide a powerful means to independently evaluate contributions from spin-allowed and/or -forbidden excited states to spin–phonon coupling terms. Furthermore, ratios between various intramolecular coupling terms for a given mode drive spin conversion processes in transition metal complexes and can be used to analyze mechanisms of ISC. Variations in geometric structure strongly influence the relative intramolecular linear spin–phonon coupling terms and will thus define the overall spin state dynamics. While of general importance for understanding magnetization dynamics, this study links the phenomenon of spin–phonon coupling across fields of single molecule magnetism, quantum materials/qubits, and transition metal photophysics.

File list (2)

Spin–Phonon Coupling and Dynamic Zero-Field Splitting Contributions to Spin Conversion Processes in Iron(II) Complexes

Nicholas J. Higdon, Alexandra T. Barth, Patryk T. Kozlowski, and Ryan G. Hadt*

Division of Chemistry and Chemical Engineering, Arthur Amos Noyes Laboratory of Chemical Physics, California Institute of Technology, Pasadena, California 91125, United States

Corresponding Author: rghadt@caltech.edu

Abstract

Magnetization dynamics of transition metal complexes manifest in properties and phenomena of fundamental and applied interest (e.g., slow magnetic relaxation in single molecule magnets (SMMs), quantum coherence in quantum bits (qubits), and intersystem crossing (ISC) rates in photophysics). While spin–phonon coupling is recognized as an important determinant of these dynamics, additional fundamental studies are required to unravel the nature of the coupling and thus leverage it in molecular engineering approaches. To this end, we describe here a combined ligand field theory and multireference *ab initio* model to define spin–phonon coupling terms in S = 2 transition metal complexes and demonstrate how couplings originate from both the static and dynamic properties of ground and excited states. By extending concepts to spin conversion processes, ligand field dynamics manifest in the evolution of the excited state origins of zero-field splitting (ZFS) along specific normal mode potential energy surfaces. Dynamic ZFSs provide a powerful means to independently evaluate contributions from spin-allowed and/or -forbidden excited states to spin–phonon coupling terms. Furthermore, ratios between various intramolecular coupling terms for a given mode drive spin conversion processes in transition metal complexes and can be used to analyze mechanisms of ISC. Variations in geometric structure strongly influence the relative intramolecular linear spin–phonon coupling terms and will thus define the overall spin state dynamics. While of general importance for understanding magnetization dynamics, this study links the phenomenon of spin–phonon coupling across fields of single molecule magnetism, quantum materials/qubits, and transition metal photophysics.

1. Introduction.

The coupling between structural and electronic degrees of freedom (e.g., spin–phonon coupling) plays critical roles in the dynamic properties of transition metal complexes. Relaxation phenomena in single molecule magnets (SMMs) and quantum bits (qubits) are thought to be strongly dependent on the coupling between vibrational modes and the electron spin M_S sublevels (e.g., $M_S = \pm ½$ for S = ½ qubits, and the zero-field split M_S sublevels for most SMMs), which can effectively modulate their relative energies and mixings.[1–8] In SMMs, these modulations can perturb magnetic anisotropy and result in lower effective barriers for relaxation (U_{eff}) and affect the tunneling of magnetization.[4,5] In qubits, ligand field modulations can result in a finite variance in the splitting of the $M_S = \pm ½$ sublevels (a reflector of molecular g values), which can give rise to decoherence in a two-level system.[8,9] Taken together, experimental and theoretical studies suggest that an increased fundamental understanding of spin–phonon coupling contributions to magnetic relaxation phenomena will provide a path towards the molecular engineering and eventual room temperature control of quantum materials for applications in quantum and classical computing. Additionally, increasing the temperature at which magnetic relaxation phenomena can be studied will open the door to more detailed studies of spin–phonon coupling in transition metal complexes. That is, at lower temperatures (<~80 K), other relaxation mechanisms (e.g., direct, Raman, Orbach) may dominate over local mode contributions, making it difficult to directly study spin–phonon couplings.[10–13]

While the phenomenon and consequences of spin–phonon coupling are of great importance for the quantum control of molecules and materials, this study is largely focused on the initial steps toward translating concepts and models to the study of spin conversion processes in transition metal complexes, including those exhibiting thermal spin crossover (SCO), light induced excited spin state trapping (LIESST), and/or ultrafast photo-triggered spin state switching in photomagnetic materials and photosensitizers. In these complexes, spin conversion processes can occur on an ultrafast timescale, even with large geometric changes, and are thus necessarily coupled to specific vibrational and/or phonon modes. These electron–phonon couplings are reflected in the potential energy surfaces (PESs) that connect the different spin states. Indeed, for photo-active transition metal complexes, ultrafast spectroscopic studies on six coordinate Fe(II) complexes have demonstrated vibrational coherences that accompany photo-triggered spin state dynamics.[14–21] This interplay between electronic and vibrational dynamics is an important factor

for directing energy relaxation pathways within transition metal complexes. For example, spin–phonon coupling represents a significant hurdle for the development of earth-abundant photosensitizers made from Fe(II) for photochemical energy conversion pathways or photoredox catalysis.[22–24] In first row transition metal complexes, excited ligand field states provide a direct relaxation pathway to the ground state. Conversely, Ru(II) and Ir(III) complexes lack low-energy ligand field transitions with which vibrational modes can couple to the initially excited metal-to-ligand charge transfer (MLCT) states (i.e., the primogenic effect[25]), which gives rise to longer MLCT excited state lifetimes.

Given these considerations, spin–phonon coupling represents a general, cross-cutting phenomenon of importance for the fundamental understanding of magnetization relaxation mechanisms in transition metal complexes for applications in spintronics, quantum materials, and/or photochemical energy conversion applications. However, it is important to develop combined experimental and computational methodologies to identify and quantify spin–phonon active modes.[3–7] Doing so will significantly aid our understanding of the origin(s) and nature of these couplings and thus allow for a more detailed rational synthetic approach to control dynamic magnetic properties in general.

While studies of spin–phonon couplings have largely considered the direct coupling between phonons and the M_S sublevels,[5,6] less focus has been on understanding the couplings through the lens of the transition metal excited state dynamics responsible for the experimental observables themselves (e.g., g values and zero-field splittings (ZFSs)).[26–28] For example, recent studies highlighted the role of ligand field excited state energies in affecting the relaxation rates of qubits at higher temperatures.[3,8,29] The excited state energy contributions are perhaps best exemplified through comparisons between vanadyl, four coordinate Cu(II), and six coordinate V(IV) complexes as molecular qubit candidates.[8] In six coordinate V(IV) complexes, the presence of low energy ligand field transitions is thought to significantly increase spin–phonon coupling terms through the introduction of ground state orbital angular momentum through excited state spin orbit coupling (SOC).[3,8] More explicitly, linear spin–phonon coupling terms in S = ½ qubit candidates are predicted to exhibit a pseudo-inverse square dependence on the ligand field transition energies and a linear dependence on the linear excited state coupling terms.[8] The relationships between linear spin–phonon and excited state coupling terms can also be used to predict and rationalize geometric dependencies on spin–lattice relaxation times in Cu(II)

complexes and qubit candidates.[8,10] Recognizing and understanding the important roles of excited state contributions to the ground state properties thus provides additional means to tune magnetic relaxation phenomena.

In contrast to considerations for qubits and SMMs, the switching between spin states in transition metal complexes introduces further interesting considerations: 1) geometric distortions upon spin conversion are typically more dramatic and thus sample more expansive regions of ground and excited PESs, and 2) as the origins of ZFS derive from excited states and their geometric perturbations, the magnitudes and partial derivatives of ZFS can thus vary quite strongly along specific vibrational modes, which necessarily requires the invocation of spin–phonon coupling. More specifically, while the ZFS at an equilibrium geometry may be largely due to spin–orbit interactions with one or two specific excited states (e.g., ^5E_g in the case of S = 2 Fe(II), *vide infra*), the relative couplings among excited and ground states can change dramatically at different locations along PESs. This is especially important for considering spin conversion processes in transition metal complexes. Thus, both the rational design of molecular magnetic materials and the understanding of photochemical energy conversion pathways requires a detailed knowledge of not only the coupling of vibrational degrees of freedom with ground state properties, but, of equal importance, the coupling of these vibrational degrees of freedom over the manifolds of ligand field excited states.

Here we provide a detailed, combined ligand field theory and multireference *ab initio* approach to understand the fundamental nature of spin–phonon couplings in S > ½ transition metal complexes, with an emphasis on linking spin–phonon coupling between molecular magnetic materials and photoactive transition metal complexes. Similar to Mirzoyan et al.,[8] this study shows that spin–phonon couplings derive from excited state coupling terms and are very sensitive to the absolute ligand field excited state energies. For specific vibrational modes, analyses can directly quantify spin–phonon coupling terms across Fe(II) complexes and demonstrate that couplings over the vibrational manifold are sensitive to the initial geometric structure of the transition metal complex (which governs the corresponding linear excited state coupling terms); accordingly, couplings can be tuned through structural perturbations to the first coordination sphere. Furthermore, while these complexes are in the ionic regime with limited ligand–metal covalency, the model described here predicts a reduction in spin–phonon coupling terms with increased covalency, similar to discussions relating to qubits.[8,30] In the limit of very low energy excited

states, or when considering orbitally degenerate excited states with in-state orbital angular momentum, significant deviations between the ligand field and *ab initio* models described here can occur. Finally, we highlight the importance of the evolution of the splittings and mixings of the M_S sublevels at intersystem crossings (ISCs) involved in spin conversion processes. While the ZFSs at S = 2 Fe(II) equilibrium geometries are largely due to a set of conserved ^5E_g excited states, the nature of the couplings and the specific excited state contributions to the energetics and dynamical properties of the M_S sublevels change dramatically along vibrational modes that facilitate ISC. The model and findings discussed here have broad impacts for the design of molecules and materials that exhibit important quantum phenomena at room temperature, as well as those involved in LIESST, SCO, photomagnetism, and solar energy conversion.

2. Results.

In the following Sections, a dynamic ligand field theory model of spin–phonon coupling terms is established that relates ground state axial ZFSs to the energetics of specific ligand field excited states. The model is then experimentally calibrated and evaluated using Fe(II) model complexes with well-defined first coordination spheres and magnetic properties. Lastly, spin–phonon coupling terms and dynamics are extended to spin conversion processes.

2.1. Dynamic Ligand Field Theory of S = 2 Fe(II) Zero-Field Splitting.

As shown in Figure 1, in O_h symmetry, the ^5D state of a d^6 S = 2 Fe(II) free ion splits into $^5T_{2g}$ ground and ^5E_g excited states separated in energy by 10Dq. An axial compression of the octahedron further splits the $^5T_{2g}$ degenerate set into a $^5B_{2g}$ ground state and a low-lying ^5E_g excited state at an energy Δ above the ground state. This corresponds to a positive ZFS, +D. Here the lower- and higher-energy ^5E_g excited states will be referred to as ^5E_g(1a,1b) and ^5E_g(2a,2b), respectively. The axial distortion can also split the ^5E_g(2a,2b) excited states into $^5A_{1g}$ and $^5B_{2g}$ states separated in energy by Δ^5E_g. For –D, the overall splittings are reversed, and the ^5E_g(1a,1b) is an orbitally degenerate ground state. Note only the +D scenario is considered here. An additional rhombic distortion can split the ^5E_g(1a,1b) excited states by an energy, V. While the S = 2 $^5B_{2g}$ ground state is orbitally nondegenerate, it is five-fold degenerate in spin. The degeneracy of the five M_S sublevels can split in the absence of a magnetic field due to excited state SOC (inset, Figure 1). Through perturbation theory and taking into account second order SOC, D can be expressed as:[31]

$$D = \frac{\lambda^2}{\Delta} = \frac{\lambda^2 \eta}{\Delta}$$

(equation 1)

where $\lambda = -\zeta/2S$ (ζ is the metal-based SOC constant), Δ is the energy weighted average of the ^5E_g(1a,1b) excited states above the ground state, and η is a parameter that accounts for the covalent reduction of $|\zeta|$. For S = 2 Fe(II), $\zeta = -400$ cm^{-1} and thus $\lambda = -100$ cm^{-1}.[32]

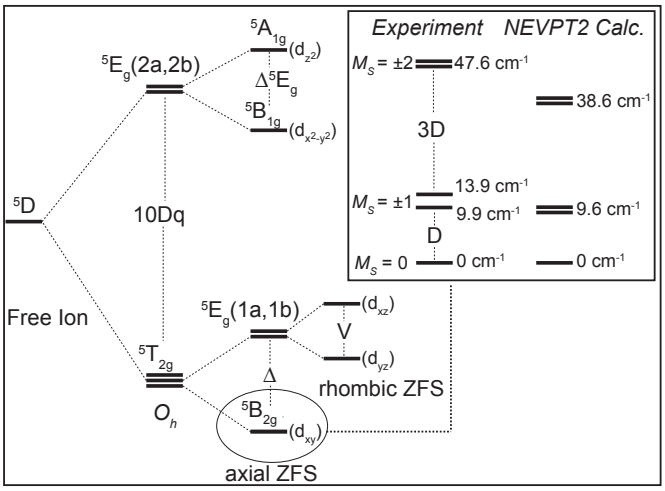

Figure 1. State splitting diagram for a d^6 S = 2 transition metal complex. Inset: Experimental M_S sublevel splittings for $FeSiF_6 \cdot 6H_2O$, $[Fe(H_2O)_6]^{2+}$, from electronic Raman spectroscopy[33] compared to the CASSCF/NEVPT2 calculated energy levels.

In order to identify and understanding the nature of spin–phonon coupling, we evaluate the change in the ZFS along specific normal modes of vibration, Q_i. Note the model described here is applicable to both phonons and vibrations, thus we simply use the terminology of spin–phonon coupling as a general description. Taking the partial derivative of equation 1 with respect to a vibrational coordinate Q_i gives:

$$\partial D/\partial Q_i = \lambda^2 \frac{\Delta\left(\partial\eta/\partial Q_i\right) - \eta\left(\partial\Delta/\partial Q_i\right)}{\Delta^2}.$$

(equation 2)

This derivative expression is referred to here as a linear spin–phonon coupling term. In the regime where $\eta\left(\partial\Delta/\partial Q_i\right) \gg \Delta\left(\partial\eta/\partial Q_i\right)$, equation 2 simplifies to:

$$\partial \mathrm{D}/\partial Q_i = \frac{\lambda^2 \eta\left(\partial\Delta/\partial Q_i\right)}{\Delta^2}.$$

(equation 3)

Thus, the linear spin–phonon coupling term is predicted to have an inverse square dependence on Δ and a linear dependence on the partial derivative in the excited state energy, $\partial\Delta/\partial Q_i$, which is directly related to the so-called linear coupling term.[34] To differentiate this term from the spin–phonon coupling term, which deals solely with the axial ZFS, D, the linear coupling term dealing with the partial derivatives of excited state energies will be referred to as a linear excited state coupling term. This term, effectively represented by the slope of the excited state PES at the nuclear coordinates of the ground state geometry, is given by:[34]

$$E^e_{elec-nuc} = \left\langle \psi_e^{elec} \middle| \left(\frac{\partial \boldsymbol{H}_{LF}}{\partial Q_i}\right)_0 \middle| \psi_e^{elec} \right\rangle Q_i.$$

(equation 4)

In addition to evaluating equation 4 at the ground state equilibrium geometry, we also evaluate the linear excited state coupling term along the ground state PES. In those cases, the linear excited state coupling term is normalized to the slope in the ground state PES.

When $\eta\left(\partial\Delta/\partial Q_i\right) \ll \Delta\left(\partial\eta/\partial Q_i\right)$, equation 2 simplifies to:

$$\partial \mathrm{D}/\partial Q_i = \frac{\lambda^2 \left(\partial\eta/\partial Q_i\right)}{\Delta}$$

(equation 5)

and $\partial D/\partial Q_i$ will have an inverse dependence on Δ and a linear dependence on the partial derivative of covalency, η. However, as shown below, the complexes considered here are quite ionic and are largely in the regime where equation 3 best describes the linear spin–phonon coupling terms. Here our aim is to emphasize the importance of the excited state energies and their linear excited state coupling terms for understanding the linear spin–phonon coupling terms, as they both play key roles in understanding spin–phonon coupling. Thus, from the above considerations, the higher the energy separation between the ^5E_g(1a,1b) states and the ground state, the lower the $\partial \mathrm{D}/\partial Q_i$ term by at least an inverse dependence.

To analyze the mechanism of ISC in Section 2.4.2, it will be useful to consider the ratio of linear spin–phonon coupling terms for two different excited states within the same molecule. Using equation 3, this ratio is:

$$\left(\partial \mathrm{D}_{ES1}/\partial Q_i\right) / \left(\partial \mathrm{D}_{ES2}/\partial Q_i\right) = n \cdot \left[\frac{\Delta(ES2)^2}{\Delta(ES1)^2}\right] \cdot \left[\frac{\left(\partial \Delta_{ES1}/\partial Q_i\right)}{\left(\partial \Delta_{ES2}/\partial Q_i\right)}\right]$$

(equation 6)

where ES1 and ES2 are two excited states that each contribute to the overall ZFS of a given transition metal complex (e.g., ^5E_g(1a,1b) and $^3T_{1g}$ states considered here) and n is a scaling factor accounting for differences in ZFS contributions from ES1 and ES2. Equation 6 thus determines the individual roles of intramolecular linear excited state and spin–phonon coupling terms to the mechanism of ISC. As shown in Section 2.4.2, for the complex considered here, equation 6 results in a pseudo-exponential variation of the ratio of linear spin–phonon coupling terms, which is an important result for understanding spin–phonon coupling and dynamic ZFS contributions to spin conversion processes in transition metal complexes.

As exemplified in our recent work on evaluating spin–phonon coupling terms in transition metal qubit candidates,[8] the parameters in the model described here are directly related to spectroscopic observables and calculable quantities. Furthermore, while this treatment is generated for O_h symmetry and distorted S = 2 Fe(II) complexes, it can be done analogously for any S > ½ transition metal complex. Lastly, the terms calculated from the equations above will be sensitive

to the absolute values of the excited state energies. Thus, a spectroscopically calibrated computational methodology is important for obtaining more quantitative insights. Below, a multireference *ab initio* approach (i.e., complete active space self-consistent field (CASSCF) N-electron valence state second order perturbation theory (NEVPT2)) is utilized to benchmark to a well-studied Fe(II) complex ($[Fe(H_2O)_6]^{2+}$) with an experimentally known axial ZFS parameter and partially defined spin-allowed and -forbidden excited state manifold. Similar *ab initio* approaches have been applied with great success to the calculation of spin Hamiltonian parameters of transition metal complexes,[6,7,35–37] including SCO complexes.[38–42] Once the methodology is applied to $[Fe(H_2O)_6]^{2+}$, it is then extended to additional complexes for the evaluation of linear spin–phonon and excited state coupling terms.

2.2. Ground and Excited State Electronic Structures of Several Fe(II) Complexes.

The ground and excited state electronic structure of the high spin S = 2 ferrous fluorosilicate (FFS, $FeSiF_6{\cdot}6H_2O$, $[Fe(H_2O)_6]^{2+}$) has been elucidated using a variety of spectroscopic methods. Magnetic susceptibility gives D = +10.9 cm^{-1},[43] which is similar to that obtained using far-infrared absorption spectroscopy (D = +11.9 and |E| = 0.67 cm^{-1}).[44,45] Electronic Raman has resolved the individual $M_S = \pm1$ sublevels at 9.9 ± 0.2 cm^{-1} and 13.9 ± 0.2 cm^{-1} and the $M_S = \pm2$ sublevels at 47.6 ± 0.2 cm^{-1} above the $M_S = 0$ level (Figure 1, inset).[33] Excited state spectroscopies, including electronic absorption[46] and magnetic circular dichroism (MCD),[47] placed the split ^5E_g excited state at 9600 and 10 800 cm^{-1} and a spin-forbidden transition (likely the lowest energy $^3T_{1g}$) at ~13 700 cm^{-1}. These data for $[Fe(H_2O)_6]^{2+}$ can be used to evaluate CASSCF/NEVPT2 calculations of the zero-field split M_S sublevels of the orbitally nondegenerate $^5B_{2g}$ ground state and the associate spin-allowed and -forbidden excited state energies.

The neutron diffraction structure of FFS corresponds to an octahedron with Fe–O bond lengths of 2.14 Å.[48] With this structure and a five 3d orbital, six electron active space with 5 quintets, 17 triplets, and 15 singlets, the axial ZFS parameter calculated using the ORCA[49,50] program is 9.6 cm^{-1}, in good agreement with experiment. The energies of the four lowest-energy M_S sublevels can also be obtained directly from the SOC corrected absorption spectrum; for this structure they are 9.6, 9.6, 38.6, and 38.6 cm^{-1}, again in fairly good agreement with experiment (Figure 1, inset). Note no rhombic ZFS is predicted for this particular structure, as all Fe–O bonds are reported as identical. Additional benchmarking calculations were carried out to test the

robustness of the active space and number of states included in the calculation. The computed results are not particularly sensitive to additional active space bonding orbitals and states (Table S1).

In addition to the zero-field split M_S sublevels, the ^5E_g(2a,2b) excited state energies were calculated to be 10 135 cm^{-1}, in good agreement with experiment (average of 10 200 cm^{-1}).[46,47] The lowest energy spin-forbidden triplet state ($^3T_{1g}$) is calculated to be at an average energy of 15 440 cm^{-1}. The lowest energy spin-forbidden singlet state, which, along with the $^3T_{1g}$, is of particular importance for ISC (*vide infra*), is calculated to be at an energy of 18 530 cm^{-1}. The ^5E_g(1a,1b) components (from the parent $^5T_{2g}$ ground state) are both calculated to be at 2100 cm^{-1}. As discussed above, the ZFS of the $^5B_{2g}$ component largely derives from the SOC of these ^5E_g(1a,1b) excited states. Accordingly, ORCA provides an estimate of the individual excited state contributions to the value of D. The ^5E_g(1a,1b) states are predicted to contribute ~5.0 cm^{-1}, while the lowest energy triplet state ($^3T_{1g}$ in O_h) is estimated to contribute ~1.8 cm^{-1}. Note that all calculated values given here and below from Section 2.2 are summarized in Table 1.

Table 1. Summary of CASSCF/NEVPT2 calculated energies for $[Fe(H_2O)_6]^{2+}$ and $[Fe(NH_3)_6]^{2+}$.

Structure	D[d]	|E/D|	$M_s = \pm1, \pm2$[d]	^5E_g (1a,1b)[d]	^5E_g (2a,2b)[d]	$^3T_{1g}$ [d]	$^1A_{1g}$ [d]
$[Fe(H_2O)_6]^{2+}$ [a]	9.6	0.003	9.6/9.6, 38.6/38.6	2100	10 135	15 440	18 530
$[Fe(H_2O)_6]^{2+}$ [b]	18.3	0.221	6.0/30.3, 73.6/77.7	635	8420	15 140	18 845
$[Fe(NH_3)_6]^{2+}$ [c]	37.9	0.101	8.5/28.0, 139.5/147.2	195	11 250	11 380	11 640
$[Fe(NH_3)_6]^{2+}$ [b]	38.4	0.072	9.8/25.2, 141/147	185	9425	13 140	15 220

[a] Neutron diffraction structure; [b] BP86 optimized structure; [c] X-ray idealized structure; [d] Average cm^{-1}

In addition to the experimental structure, a full geometry optimization using the BP86 functional was carried out starting from the neutron diffraction structure of $[Fe(H_2O)_6]^{2+}$. Notably, the BP86 optimized structure features a slight axial compression along the z-axis (2.13 vs. 2.14 Å) and a slight elongation of the equatorial Fe–O bonds (2.16 vs. 2.14 Å). Using the optimized structure, the axial ZFS is calculated to be 18.3 cm^{-1}, increased relative to 9.6 cm^{-1} from the neutron diffraction structure. The M_S sublevels from the SOC corrected absorption spectrum are at 6.0, 30.3, 73.6, and 77.7 cm^{-1}. The larger and smaller magnitudes of the splittings of the $M_S = \pm1$ and ±2 sublevels, respectively, is qualitatively consistent with experiment (Figure 1, Inset). The calculated ^5E_g(2a,2b) and ^5E_g(1a,1b) states are at 8065/8770 cm^{-1} and 545/720 cm^{-1}, respectively,

while the triplet and singlet states are 15 140 cm^{-1} and 18 845 cm^{-1}, respectively. Overall, the increased ZFS for this structure relative to the neutron diffraction structure is consistent with lower energy ^5E_g(1a,1b) states, which contribute ~15.8 cm^{-1} to the total axial ZFS, with a small ~0.8 cm^{-1} contribution from the lowest energy triplet.

For direct comparison to $[Fe(H_2O)_6]^{2+}$, calculations were extended to $[Fe(NH_3)_6]^{2+}$. Experimental structures for $[Fe(NH_3)_6]^{2+}$ have been reported with Fe–N bond distances varying from ~2.21 – 2.23 Å depending on the counterion.[51–53] Thus, we used a semi-idealized structure here, which has Fe–N bond distances of 2.22 Å. For this structure, the axial ZFS of $[Fe(NH_3)_6]^{2+}$ is calculated to be significantly larger than the neutron diffraction $[Fe(H_2O)_6]^{2+}$ structure (37.9 vs. 9.6 cm^{-1}). The M_S sublevels are at 8.5, 28.0, 139.5, and 147.2 cm^{-1}. Experimentally, bands at 12 400 and 9000 cm^{-1} have been assigned to components of the $^5T_{2g} \rightarrow {}^5E_g$(2a,2b) transition.[54] Here, for the X-ray idealized structure, the ^5E_g(2a,2b) and ^5E_g(1a,1b) states are calculated at 11 250/11 255 cm^{-1} and 145/240 cm^{-1}, respectively, while the lowest energy triplet and singlet states are 11 380 cm^{-1} and 11 640 cm^{-1}, respectively. The relatively large ZFS for the X-ray idealized structure of $[Fe(NH_3)_6]^{2+}$ is consistent with a the low energies of the ^5E_g(1a,1b) states, which contribute ~31.6 cm^{-1} to the total axial ZFS, with a small ~1.6 cm^{-1} contribution from the lowest energy triplet.

As for $[Fe(H_2O)_6]^{2+}$, a BP86 fully optimized structure was also obtained for $[Fe(NH_3)_6]^{2+}$. Upon optimization, the Fe–N bonds expand to 2.31/2.30 Å and 2.28/2.28/2.29/2.29 Å in the axial and equatorial planes, respectively. The computed axial ZFS for the optimized structure is slightly larger than that of the idealized structure (38.4 vs. 37.9 cm^{-1}, respectively), with ~32.4 and ~1.1 cm^{-1} of the ZFS deriving from the ^5E_g(1a,1b) and $^3T_{1g}$ states, respectively. The M_S sublevels are at 9.8, 25.2, 141.0, and 147.0 cm^{-1}. The ^5E_g(2a,2b) and ^5E_g(1a,1b) states are predicted at 9235/9615 cm^{-1} and 155/210 cm^{-1}, respectively, while the triplet and singlet states are 13 140 cm^{-1} and 15 220 cm^{-1}, respectively. Overall, upon optimization and expansion of the Fe–N bonds, the energies of the ^5E_g(1a,1b) states do not change as dramatically as the ^5E_g(2a,2b) states, which is consistent with similar computed axial ZFS values between the two structures.

2.3 Spin–Phonon Coupling Terms.

2.3.1. Identifying Coupling Modes.

The 15 normal modes of vibration of an octahedron include: $\Gamma_{vib} = a_{1g} + e_g + t_{2g} + 2t_{1u} + t_{2u}$. The a_{1g}, e_g, and one t_{1u} set of modes are stretches and the other t_{1u}, t_{2u}, and t_{2g} modes are bends (Figure

S1). Calculated frequencies and distortion vectors for the neutron diffraction and BP86 optimized structures of $[Fe(H_2O)_6]^{2+}$ are given in Tables S2 and S3, respectively. As mentioned above, the Fe–O bond distances for the experimental structure are all equivalent (2.14 Å), while the BP86 optimized structure features a slight compression along the z-axis (2.128 Å) and elongation in the equatorial plane (2.161 and 2.166 Å for x- and y-axes, respectively). As discussed below, this distortion upon geometry optimization corresponds to the $e_g(\theta)$ component of the e_g stretching vibrations (Figure 2). For the neutron diffraction structure, there are 18 imaginary frequencies that correspond to water-based waging and rocking motions. However, all 15 modes of the octahedron have positive frequencies up to ~340 cm^{-1} (Table S2). For the purposes of this study, the absolute energies of the modes are not as important as the absolute atomic displacements, and the 15 modes considered here are all components of the normal modes of an octahedron.

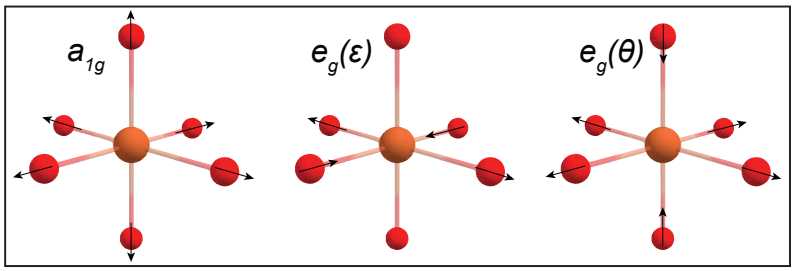

Figure 2. Three key ML_6 O_h normal modes.

The BP86 optimized structure represents a minimum energy structure with no imaginary frequencies. 26 normal modes are computed with energies <400 cm^{-1}. 15 of these modes are those of the octahedron (Table S3). The other 11 normal modes in this energy region correspond to water-based motions with little to no M–L-based motion. Below, we focus solely on M–L based bends and stretches.

Spin–phonon coupling terms were calculated as described in the Computational Methods section of Supporting Information. Briefly, to estimate the qualitative magnitudes of spin–phonon coupling terms, the axial ZFS parameter, D, was calculated along all normal modes of vibration. In addition to D, the energies of the ^5E_g(1a,1b) excited states are also followed. These calculations are presented in Figures 3A – 3H. For the neutron diffraction structure, two of the 15 modes of the octahedron exhibit appreciable linear spin–phonon coupling terms. These are the totally symmetric stretch (a_{1g}, Figure 3A) and a component of the t_{2g} bending mode (purple markers in Figure 3).

The absolute values of the slopes are 4.4 and 1.1 cm^{-1}/Q_i for the a_{1g} mode and the bending mode, respectively. For more quantitative analyses (*vide infra*), it is convenient to convert, when possible, the slope to a $Å^{-1}$ scale. The absolute value of the slope for the a_{1g} mode is 18.5 $cm^{-1}/Å$.

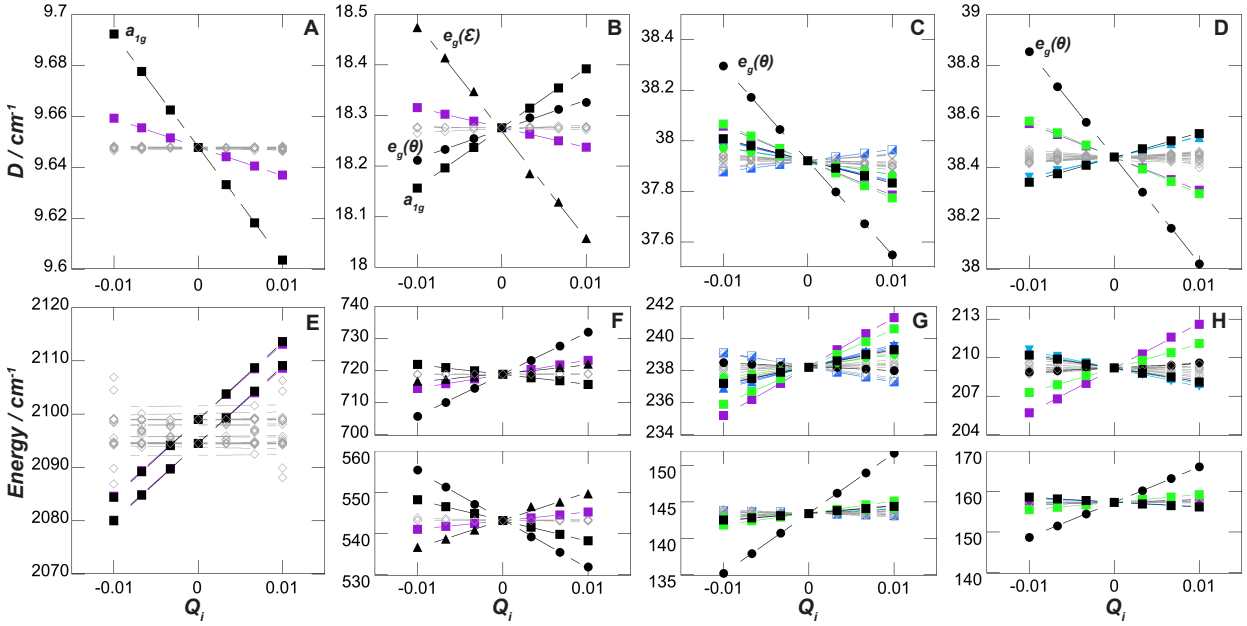

Figure 3. Linear spin–phonon (A – D) and excited state (E – H) coupling term calculations for the neutron diffraction structure (A, E) and BP86 optimized (B, F) structures of $[Fe(H_2O)_6]^{2+}$ and the X-ray crystallographic-based (C, G) and BP86 optimized structure (D, H) of $[Fe(NH_3)_6]^{2+}$.

For further analyses, we turn to the excited state linear coupling term introduced in Section 2.1. This term is represented by the slope of the excited state PES at the nuclear coordinates of the ground state geometry. When nonzero, a force is present on the excited state geometry, which will distort the structure along a normal mode by ΔQ_i to lower the total energy. Thus, the linear excited state coupling term can be used to evaluate $^{\partial \Delta}/_{\partial Q_i}$ discussed above. Importantly, while the ZFS is a ground state property, it reflects contributions from excited state PESs and SOC contributions. Thus, modes that exhibit linear spin–phonon coupling terms should exhibit appreciable linear excited state coupling terms. Indeed, by comparing Figure 3A and 3E, the a_{1g} and bending mode also exhibit corresponding linear excited state coupling terms, while other modes do not (they are quadratic). Note fits and/or slopes in Figure 3 are provided in Tables S4 – S11. Thus, the

corresponding dynamic changes in ground state ZFS can be directly linked to dynamic contributions from distorted excited state PESs.

Ground state linear spin–phonon and excited state coupling terms for the BP86 optimized structure of $[Fe(H_2O)_6]^{2+}$ are given in Figures 3B and 3F. Interestingly, additional modes exhibit linear coupling terms and thus become activated for this structure. In addition to the a_{1g} mode and a bending mode, both e_g stretching modes exhibit appreciable slopes. The vector displacements for the $e_g(\theta)$ and $e_g(\varepsilon)$ components are represented in Figure 2. The axial ZFS slopes are 21.2, 11.8, 5.8, and 3.9 cm^{-1}/Q_i for the $e_g(\varepsilon)$, a_{1g}, $e_g(\theta)$, and bending mode, respectively.

The results for the neutron diffraction and BP86 structures provide a convenient comparison between coupling terms. For the neutron diffraction structure, the linear spin–phonon coupling term for the a_{1g} mode was 4.4 cm^{-1}/Q_i, which equated to 18.5 cm^{-1}/Å. The linear spin–phonon coupling terms for the optimized structure were 11.8 cm^{-1}/Q_i, or 50.7 cm^{-1}/Å, which is significantly larger than the neutron diffraction structure. The increased linear spin–phonon coupling term for the BP86 structure derives from the significantly lower energy ^5E_g(1a,1b) states (545/720 cm^{-1}) relative to those for the neutron diffraction structure (2095/2100 cm^{-1}), in accord with the model described in Section 2.1. Furthermore, the linear excited state coupling terms for the e_g modes in the neutron diffraction structure exhibit no appreciable slope (Figure 3E). Rather, they exhibit quadratic coupling. This behavior is in distinct contrast to the appreciable linear excited state coupling terms for the BP86 structure (Figure 3F). Thus, the presence of new excited state linear coupling terms for the optimized structure gives rise to appreciable ground state linear spin–phonon coupling terms for new modes. This result is of general importance for considering the roles of geometric and electronic structure on the nature of spin–phonon coupling in transition metal complexes.

Calculations on the two different forms of $[Fe(H_2O)_6]^{2+}$ were extended to two structures of $[Fe(NH_3)_6]^{2+}$. Similar to $[Fe(H_2O)_6]^{2+}$, the first structure considered was derived from X-ray crystal structures. There are several modes that exhibit linear spin–phonon coupling terms. The absolute values of the largest slopes are 37.4, 14.6, 13.6, and 8.7 cm^{-1}/Q_i, which correspond to the $e_g(\theta)$, a stretching, a bending, and the a_{1g} modes, respectively. The corresponding excited state linear coupling terms are given in Figure 3G. For the a_{1g} mode, the linear spin–phonon coupling term equates to 41.6 cm^{-1}/Å. Again, the larger spin–phonon coupling term for this structure derives from the low energies of the ^5E_g(1a,1b) states (145/240 cm^{-1}).

Spin–phonon coupling term calculations were finally extended to the optimized structure of $[Fe(NH_3)_6]^{2+}$ (Figure 3D). The absolute values of the largest slopes are 41.6, 14.2, 13.1, and 9.6 cm^{-1}/Q_i, which correspond to the $e_g(\theta)$, a stretching, a bending, and the a_{1g} modes, respectively. The corresponding linear excited state coupling terms are given in Figure 3H. For the a_{1g} mode, the spin–phonon coupling term equates to 45.3 cm^{-1}/Å. Again, the larger spin–phonon coupling term derives from the low energies of the ^5E_g(1a,1b) states (155/210 cm^{-1}).

2.3.2. Quantitative Spin–Phonon Coupling Comparisons.

With the ability to obtain linear spin–phonon and excited state coupling terms for the a_{1g} modes of multiple structures, direct comparisons can be made with the expressions given in Section 2. From Löwdin orbital population analyses, the dπ and dσ orbital characters for $[Fe(H_2O)_6]^{2+}$ and $[Fe(NH_3)_6]^{2+}$ structures are similar and ~95 %, respectively. Thus, they are in the regime where equation 3 is most appropriate for describing linear spin–phonon coupling terms. The first example will compare results from the neutron diffraction and BP86 optimized structures of $[Fe(H_2O)_6]^{2+}$. For these, the linear spin–phonon coupling terms were calculated to be 18.5 and 50.7 cm^{-1}/Å, respectively (a ratio of 0.365). Using equation 3 (equating $\lambda^2\eta$ for both structures), the calculated values of Δ (the energies of ^5E_g(1a,1b)), and the linear excited state coupling terms (slopes of the ^5E_g(1a,1b) states), we estimate an overall ratio of linear spin–phonon coupling terms of 0.364 for the a_{1g} mode, in agreement to that calculated directly using the ratios of the linear spin–phonon coupling terms. Note the value of 0.364 is obtained by using equation 3 and using the average contributions from both ^5E_g(1a,1b) states (i.e., 0.190 and 0.538 for ^5E_g(1a) and ^5E_g(1b) states, respectively) (Table 2).

Table 2. Spin–Phonon Analyses for the a_{1g} Mode of Multiple Fe(II) Complexes.

Structure	D[d]/Å	^5E_g(1a)[d]	^5E_g(1b)[d]	^5E_g(1a) /Å	^5E_g(1b) /Å	Ratio[e]	Ratio(1a)[f]	Ratio(1b)[f]	Ratio (ave)[f]
States	5 quintets, 17 triplets, 15 singlets								
$[Fe(H_2O)_6]^{2+}$ [a]	18.5	2095	2100	6079	6095	1	1	1	1
$[Fe(H_2O)_6]^{2+}$ [b]	50.7	545	720	2147	1330	0.365	0.190	0.538	0.364
$[Fe(NH_3)_6]^{2+}$ [c]	41.6	145	240	460	510	0.445	0.062	0.154	0.108
$[Fe(NH_3)_6]^{2+}$ [b]	45.3	155	210	585	500	0.408	0.058	0.180	0.090
States	3 quintets, 0 triplets, 0 singlets								
$[Fe(H_2O)_6]^{2+}$ [a]	17.8	2050	2050	5965	5950	1	1	1	1
$[Fe(H_2O)_6]^{2+}$ [b]	56.4	530	700	2125	1275	0.316	0.185	0.543	0.364
$[Fe(NH_3)_6]^{2+}$ [c]	39.0	150	245	455	470	0.456	0.069	0.180	0.125
$[Fe(NH_3)_6]^{2+}$ [b]	43.2	160	205	595	410	0.412	0.060	0.146	0.103
States	5 quintets, 0 triplets, 0 singlets								
$[Fe(H_2O)_6]^{2+}$ [a]	22.4	2030	2030	5915	5925	1	1	1	1
$[Fe(H_2O)_6]^{2+}$ [b]	55.3	520	690	2135	1290	0.405	0.182	0.528	0.355
$[Fe(NH_3)_6]^{2+}$ [c]	36.6	145	235	430	460	0.612	0.070	0.174	0.122
$[Fe(NH_3)_6]^{2+}$ [b]	40.1	155	200	570	400	0.559	0.060	0.140	0.100

[a] Neutron diffraction structure; [b] BP86 optimized structure; [c] X-ray idealized structure; [d] cm^{-1}; [e] from D/Å directly; [f] from equation 3

The same approach can be extended to the X-ray idealized and BP86 optimized structures of $[Fe(NH_3)_6]^{2+}$. The ratios of their linear spin–phonon coupling terms relative to the neutron diffraction structure of $[Fe(H_2O)_6]^{2+}$ are 0.445 and 0.408, respectively. Using equation 3, ratios of 0.108 and 0.090 are obtained. Notably, the ratios obtained from equation 3 differ significantly from the ratios obtained using the absolute values of the linear spin–phonon coupling terms. As discussed below in Section 2.3.3, we assign these deviations for $[Fe(NH_3)_6]^{2+}$ to the significantly lower energies of the ^5E_g(1a,1b) states relative to the $[Fe(H_2O)_6]^{2+}$ structures (e.g., 143/238 cm^{-1} and 157/209 cm^{-1} for the X-ray idealized and BP86 optimized structures of $[Fe(NH_3)_6]^{2+}$, respectively). Thus, for $[Fe(NH_3)_6]^{2+}$, equation 3 predicts significantly larger spin–phonon coupling terms than those obtained directly from axial ZFS values.

Lastly, the analysis in this section has utilized 5 quintets, 15 triplets, and 17 singlets, respectively. The same analyses can be done only considering three or five quintets to determine the extent to which other excited states can contribute to the linear spin–phonon coupling terms at the equilibrium geometries. Using three quintet states, the ratio of spin–phonon coupling terms in the case for the $[Fe(H_2O)_6]^{2+}$ structures is 0.316, compared to a value of 0.364 using equation 3 (middle entries in Table 2). Using five quintets, the ratio is 0.355. Thus, better agreement between the absolute spin–phonon coupling terms and those obtained from equation 3 can be obtained by including spin-forbidden excited states (triplets in this case). Generally, the relative excited state contributions to the linear spin–phonon coupling terms will depend on the initial relative magnitudes of individual excited state linear coupling terms.

2.3.3. Deviation of D and Spin–Phonon Coupling Terms from Model Behavior.

As shown above, more quantitative analyses of spin–phonon and excited state coupling terms indicated that $[Fe(NH_3)_6]^{2+}$ deviated from the model described in Section 2, while $[Fe(H_2O)_6]^{2+}$ provided excellent agreement. This behavior can be understood through further analyses of the nature of the ZFS as a function of Δ. When Δ is <~500 cm^{-1}, the axial ZFS is not well-described by equation 1.[31] Rather, deviations from equation 1 can occur due to the presence of in-state orbital angular momentum deriving from the parent $^5T_{2g}$ state, which necessitates the use of a full spin Hamiltonian including SOC over all components of the $^5T_{2g}$ ground state. Indeed, the average values of Δ for the $[Fe(H_2O)_6]^{2+}$ structures are 2095 and 635 cm^{-1} for the neutron diffraction and optimized structures, respectively. The analogous values for the X-ray and optimized structures of

$[Fe(NH_3)_6]^{2+}$ are 190 and 180 cm^{-1}, respectively, well below 500 cm^{-1}. Thus, for the $[Fe(NH_3)_6]^{2+}$ structures, we ascribe the deviations of linear spin–phonon coupling terms from equation 1 to the increased in-state orbital angular momentum from the low energies of the ^5E_g(1a,1b) states.

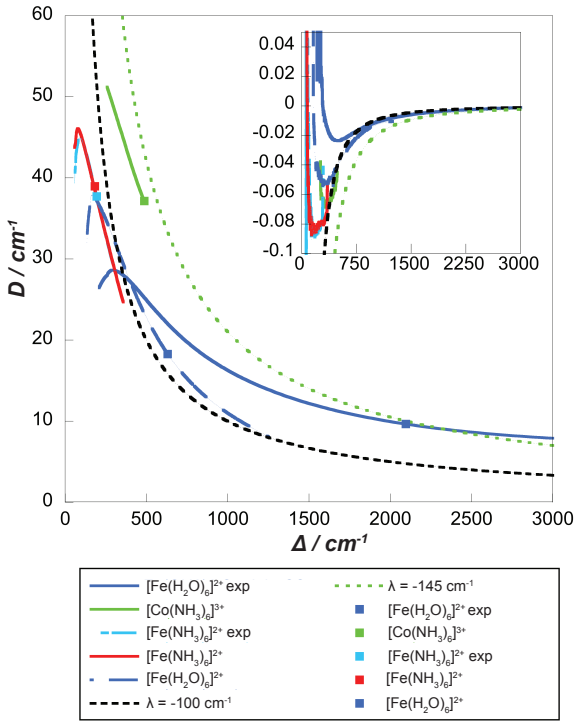

Figure 4. Variations of +D vs. Δ (the energies of the ^5E_g(1a,1b) states given in Figure 1) using equation 1 for different values of λ (dashed black and dashed green lines) compared to CASSCF/NEVPT2 computed values. (Inset) Magnitude of the first derivative of the D vs. Δ. In the legend, exp represents data for the neutron diffraction and the X-ray crystallographically derived structures of $[Fe(H_2O)_6]^{2+}$ and $[Fe(NH_3)_6]^{2+}$, respectively.

To gain further insights into the direct calculation of linear spin–phonon coupling terms and to better understand the behavior of the CASSCF/NEVPT2 calculated axial ZFS as a function of Δ, the totally symmetric a_{1g} mode can be used as a means to determine the functional form of D vs. Δ (Figure 4A). The variation in D as a function of Δ, as predicted by equation 1 (λ = –100 cm^{-1}), is given in Figure 4A (black line). The CASSCF/NEVPT2 calculated correlations for $[Fe(H_2O)_6]^{2+}$ and $[Fe(NH_3)_6]^{2+}$ are also given in Figure 4A. For comparison, we also provide the correlation generated using the BP86 optimized geometry of the high spin form of $[Co(NH_3)_6]^{2+}$

(green line, Figure 4A) (the structure obtained here is consistent with the excited state distorted structure given by Solomon and coworkers[55]). From equation 1, D increases due to the increased SOC constant of Co(III) (580 cm^{-1}) relative to Fe(II) (400 cm^{-1}). Note that the shapes of the calculated traces relative to that from equation 1 are similar to those obtained from the full spin Hamiltonian including SOC over all components of the $^5T_{2g}$ ground state.[31] The first derivatives of D vs. Δ are given in the inset of Figure 4. Significant deviations from equation 1 are observed below ~500 cm^{-1}, around which the value of D does not continue to increase but even slopes downwards in energy (consistent with the full spin Hamiltonian description[31]). These deviations can thus give rise to deviations between the linear spin–phonon coupling terms estimated by equation 1 and those from CASSCF/NEVPT2 calculations (i.e. the left- and right-hand sides of equations 2 and 3, respectively).

2.4. Extension to the $^1A_{1g}/^5T_{2g}$ ΔS = 2 ISC.

2.4.1. SCO Through the Lens of ZFS.

A Tanabe-Sugano-like diagram generated with the a_{1g} mode for the $[Fe(H_2O)_6]^{2+}$ neutron diffraction structure is given in Figure 5A. As expected, a clear change in ground state spin occurs along the a_{1g} breathing mode. Given the CASSCF/NEVPT2 methodology can quantitatively follow the energetic evolution of the ZFS and low-lying M_S sublevels of the ground state, we sought to explore and analyze the mechanism of ISC. To do so, the energies of the five M_S sublevels of the ground state and the $^1A_{1g}$ excited state were followed with high resolution steps near the ISC (Figure 5B). Note the lowest M_S sublevel is set to zero energy in Figure 5. An a_{1g} PES without normalizing to the ground state energy is also given in Figure 6A. From Figure 5, the $^1A_{1g}$ excited state (black line) approaches the $M_S = \pm2$ and ±1 sublevels (green and purple lines) and then crosses the $M_S = \pm2$ sublevels. However, ISC (as deduced from the lowest energy component of the CASSCF/NEVPT2 transition energies) does not occur until some point after the $^1A_{1g}$ excited state continues to approach the $M_S = \pm1$ sublevels (red line in Figure 5B). Furthermore, as the $^1A_{1g}$ state approaches the orbitally nondegenerate ground state along the a_{1g} PES, it undergoes mixing with the lowest energy M_S component, as shown by the brown dashed line in Figure 5B. This increase in $^1A_{1g}$ excited state contribution to the lowest energy, ground state M_S sublevel occurs with a concomitant decrease in the $^1A_{1g}$ contribution to the original $^1A_{1g}$ excited state (black dashed line). Note the energy separation between the lowest energy M_S sublevel and

the original $^1A_{1g}$ state at ISC is ~100 cm^{-1}, which we tentatively describe as the electronic coupling term, V (not the rhombic ZFS V). This value is consistent with values considered previously for describing spin conversion processes in Fe(II) complexes.[56,57] As discussed further below, while only the a_{1g} PES is followed here, other vibrational modes will likely play important roles in perturbing this picture and facilitated the overall mixings. For example, McCusker et al.[58] and Purcell[59] discuss the role of trigonal twisting modes. In principle, all the different mode contributions can be determined by evaluating the linear spin–phonon and excited state coupling terms along each vibrational mode.

As the $^1A_{1g}$ and $^5T_{2g}$ states differ by $\Delta S = 2$, no matrix elements connect them directly. However, nonzero matrix elements exist between both the $^1A_{1g}$ and $^5T_{2g}$ states with the $^3T_{1g}$ state. Because of this, the triplet is thought to mediate the ISC.[56] The $^1A_{1g}$ mixings described above can be probed by following the same PES without triplet states (e.g., 5 quintets and 15 singlets). Doing so eliminates the mixing of the $^1A_{1g}$ excited into the ground state M_S sublevel (Figure S2).

In addition to understanding the $^1A_{1g}$ state contributions over the ground state M_S sublevels, the individual contributions to the overall ZFS from quintet, triplet, and singlet states along the a_{1g} PES can be evaluated (Figure 5C). As mentioned above, the quintet states are the major contributor to +D at the equilibrium geometry. However, as the structure evolves along the a_{1g} PES, the percent contribution to D from the triplets increases dramatically. Indeed, just before the $^1A_{1g}$ state crosses the $M_S = \pm 2$ sublevels (~1.871 Å Fe–O bond distance), the major contribution to the ZFS is from the triplet states (~70 %), with a significantly smaller contribution from the quintets (30 %) (Figure 5C). Also, after the $^1A_{1g}$ state crosses the $M_S = \pm 2$ sublevels, just before ISC, even the singlet states contribute a small amount to D (Figure 5C, inset). Thus, in this case, while ISC is not mediated by the triplet excited state through a direct population, the overall contributions to the ZFS reflect a dominant triplet component ($^3T_{1g}$) from excited state SOC. This increased triplet component further allows for the $^1A_{1g}$ mixing into the ground state M_S sublevels, facilitating ISC.

In summary, the magnitude and nature of the ZFS evolves significantly along the a_{1g} PES. This necessarily requires concomitant changes in the magnitudes and natures of the linear spin–phonon coupling terms. These observations stem directly from the dynamic nature of the linear excited state coupling terms over the potential energy landscape. This method, employing CASSCF/NEVPT2 calculations and analyses, represents a powerful means to dissect the mechanisms of SCO and ISCs in transition metal dynamics and photophysics.

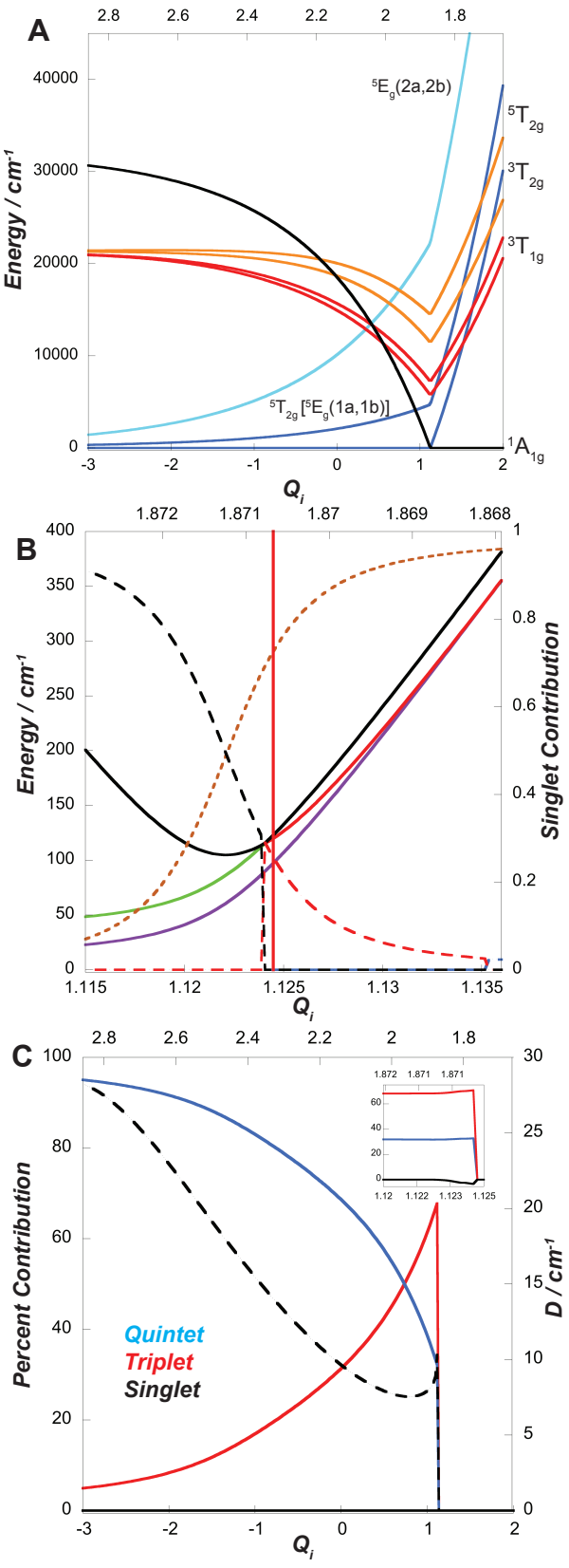

Figure 5. Electronic structural changes along the a_{1g} mode of the neutron diffraction structure of $[Fe(H_2O)_6]^{2+}$. (A) CASSCF/NEVPT2 calculated Tanabe-Sugano-like diagram for select states. (B) Variations in the of the $^1A_{1g}$ state (black solid line) and the M_S sublevels of the orbitally nondegenerate ground state (green and purple solid lines). Total singlet contributions to the $^1A_{1g}$ excited state (black dashed line) and the lowest energy M_S sublevel (brown dashed line) are overlaid. (C) Variations in the percent contributions to +D along the a_{1g} mode. The break occurs at the ISC. (Inset) Zoom in of the region near SCO. Top x-axis units: Å.

2.4.2. A Spin–Phonon Coupling-Based Mechanism of ISC.

As discussed above, the M_S sublevels of the orbitally nondegenerate component of the S = 2 ground state undergo mixing with the $^1A_{1g}$ excited state along the a_{1g} vibrational coordinate. This mixing is facilitated by the $^3T_{1g}$ state. Thus, here, using the neutron diffraction structure of $[Fe(H_2O)_6]^{2+}$, we further consider the role of spin–phonon coupling in facilitating ISC. We've approached this with the following steps: 1) the energies of the $^1A_{1g}$, ^5E_g(1a,1b), and the $^3T_{1g}$ states were calculated along the a_{1g} PES (Figure 6A). Note this provides an activation energy, E_a, of ~6700 cm^{-1} for $^1A_{1g} \rightarrow {}^5T_{2g}$ ISC. This value will be used for further analyses presented below. 2) The ZFS and its derivative were calculated along the a_{1g} PES (Figure 6B). While the ZFS ranges from ~7 – 15 cm^{-1} along this PES, there is a dramatic increase in ZFS and the corresponding linear spin–phonon coupling term as the structure approaches the ISC. Given the PES is along the a_{1g} mode, we can convert the distortion to a $Å^{-1}$ scale. 3) Using this, linear excited state coupling terms for the ^5E_g(1a,1b) and $^3T_{1g}$ states along the a_{1g} PES can be obtained. Note the $^3T_{1g}$ state splits into a lower-energy nondegenerate ($^3T_{1g}$(1a)) and higher energy degenerate set of states ($^3T_{1g}$(1b,1c)). Near the ISC, it is $^3T_{1g}$(1a) that largely contributes to +D, while the other $^3T_{1g}$(1b,1c) states contribute negatively. 4) Linear spin–phonon coupling terms were then calculated for the ^5E_g(1a,1b) and $^3T_{1g}$(1a) states along the a_{1g} PES. 5) The ratios of the linear spin–phonon coupling terms between the ^5E_g(1a) and $^3T_{1g}$(1a) states were then evaluated along the a_{1g} PES (Figure 6C, red line) (i.e., using the right hand side of equation 6). Interestingly, this ratio of linear spin–phonon coupling terms (^5E_g(1a,1b)/$^3T_{1g}$(1a)) varies in a pseudo-exponential fashion over the a_{1g} PES, with a significant decrease in the ratio as the structure approaches the ISC due to the increased contribution from the $^3T_{1g}$(1a) state and decreased contribution from the ^5E_g(1a,1b) states (also shown in Figure 5C). 6) The ratios of the linear spin–phonon coupling terms were also determined independently using the ZFS values calculated using the CASSCF/NEVPT2 approach (i.e., the left hand side of equation 6). Thus, the ratios obtained using both sides of equation 6 can be compared directly (Figure 6C, red vs. black lines, respectively; a scaling factor, n, of 0.1 was employed here for the right-hand side of equation 6).

Over the majority of the a_{1g} scan, the agreement between the two sides of equation 6 is poor (Figure 6C, red vs. black line). However, the agreement improves dramatically nearer the region of ISC. As outlined above in Section 2.3.3 for $[Fe(H_2O)_6]^{2+}$ vs. $[Fe(NH_3)_6]^{2+}$, the disagreement with equation 2 for these structures derived from the presence of in-state orbital

angular momentum. Since the $^3T_{1g}$ state is three-fold orbitally degenerate, it will contain in-state orbital angular momentum, the magnitude of which should be larger for a free ion vs. that in a complex. Accordingly, the three components of the $^3T_{1g}$ are split in energy along the a_{1g} PES, which quenches the in-state orbital angular momentum (Figure 6C, Inset C.2). Thus, better agreement between the left- and right-hand sides of equation 6 is obtained when in-state orbital angular momentum is quenched by the structural distortion. This observation further suggests that in-state orbital angular momentum can contribute to the magnitude of spin–phonon coupling terms and thus the resulting magnetization dynamics.

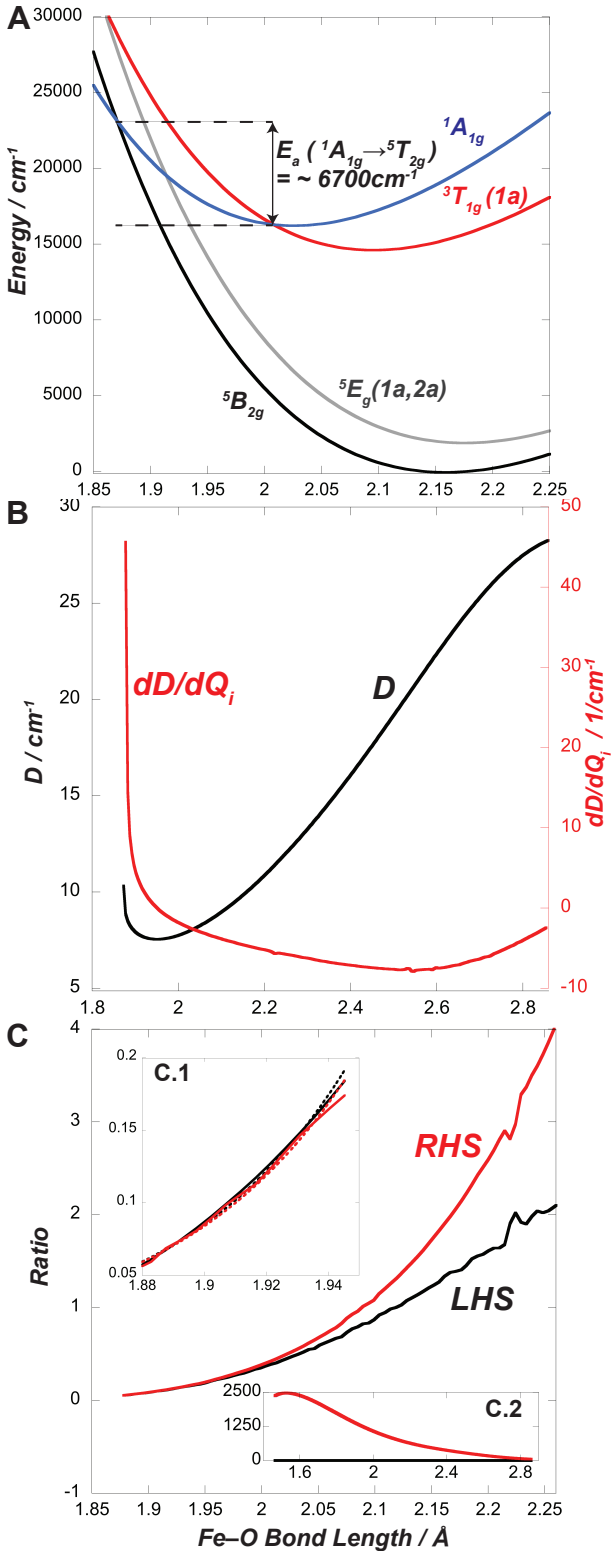

Figure 6. Variations of ligand field and spin Hamiltonian parameters along the a_{1g} mode of the $[Fe(H_2O)_6]^{2+}$ neutron diffraction structure. (A) Ground and excited state PESs relevant for the $\Delta S = 2$ ISC. (B) Variation of D (black line) and its first derivative. (C) Ratio of the linear spin–phonon coupling terms computed using the LHS (black line) and RHS (red line) of equation 6. (Inset, C.1) Zoom in of the ratios near the ISC, including exponential fits (dotted lines) ($R^2 = >0.99$). (Inset, C.2) Energy splitting in cm^{-1} of the orbitally degenerate $^3T_{1g}$ state (in O_h). The lowest energy component (black line) is normalized to zero energy.

Given the variation in the ratios of the ^5E_g(1a,1b) and $^3T_{1g}$(1a) linear spin–phonon coupling terms appear to change in a pseudo-exponential fashion, we fit the change in the ratio near the ISC for the results from the left- and right-hand sides of equation 6 (Figure 6C, Inset C.1). Note the data in Figure 6C have been converted to $Å^{-1}$. For the right hand side, the fit provides an exponent of 17.492, while a value of 17.150 is obtained from the fit of the left hand side. While the ratio of linear spin–phonon coupling terms is unitless, it is interesting to calculate an apparent activation energy, E_a, assuming an Arrhenius model. Converting the exponent to energy and multiplying by the approximate Fe–O bond distance near the ISC (~1.878 Å taken here) provides energies of ~6605 and ~6735 cm^{-1} for the left- and right-hand sides of equation 6, respectively. Interestingly, the E_a determined in this way is very similar to that of ~6700 cm^{-1} given in Figure 6A for the $^1A_{1g}$ → $^5T_{2g}$ interconversion. Note the E_a determined from the ratio of intramolecular spin–phonon coupling terms does not feature the $^1A_{1g}$ energy directly; rather, the model only takes into account the dynamic ZFS contributions from the ^5E_g(1a,2a) and $^3T_{1g}$ states near the ISC. We do not claim this to be a general means of determining an E_a, but it is interesting to note this observation in passing here within the broader context of the model. It will be of interest to consider this further and whether the model can accurately describe apparent activation energies obtained from variable temperature rates of Fe(II) ISCs measured using transient absorption spectroscopy.[57,58,60,61]

In summary, the ratios of intramolecular spin–phonon coupling terms reflect dynamic ZFS contributions along vibrational PESs and form the basis for a spin–phonon coupling-based model of ISC. The ratios determined using the left- or right-hand sides of equation 6 are also sensitive to the amount in-state orbital angular momentum in the specific excited states that govern the spin–phonon coupling terms. These dynamic ZFSs drive ISC in transition metal complexes, and future studies will be directed at extending the model to other Fe(II) complexes and transition metal ISC dynamics in general.

3. Discussion.

The phenomenon of spin–phonon coupling manifests in a wide array of important aspects of transition metal dynamics. Here we have developed a combined ligand field theory model and CASSCF/NEVPT2 computational approach to identify and describe linear spin–phonon coupling terms for S = 2 Fe(II) complexes with +D. This description allows for the determination of the ligand field excited state origin of ground state linear spin–phonon coupling terms, which are quite

sensitive to the geometric and electronic structure of the complex. As such, the overall coupling terms can vary significantly for specific normal modes (e.g., a_{1g}, $e_g(\theta)$, and $e_g(\varepsilon)$ modes). Variations in coupling terms can furthermore activate modes in a complex that were inactive in others. We've further shown that the ligand field theory model described in Section 2 can break down when significant in-state orbital angular momentum is present (e.g., for very low energy excited states (^5E_g(1a,1b) in this study) or when couplings are mediated by orbital triplets (e.g., $^3T_{1g}$). Nonetheless, direct comparisons with multireference *ab initio* calculations allow for significant insights into the nature of spin–phonon coupling and the model is directly translatable to other transition metal complexes.

3.1. Covalency Contributions. While complexes considered here are in an ionic regime, it will be of interest to extend the models to complexes that exhibit higher degrees of covalency. For example, anisotropic covalency has been shown to contribute significantly to the ZFSs in transition metal complexes (e.g., $[FeCl_4]^-$ and $[Co(SPh)_4]^{2-}$).[26,27,35]

3.2. Experimental Considerations. Additional questions remain as to how spin–phonon coupling terms can be qualitatively or quantitatively evaluated experimentally. A recent study utilizing magnetic field dependent Raman and far-IR studies have observed avoided crossings, which have been utilized to evaluate and quantify spin–phonon coupling.[6,7] However, it should be noted that the linear spin–phonon coupling terms discussed here are fundamentally different than the couplings discussed in these references, as they deal with the case where a vibrational mode and an M_S sublevel are nearly degenerate and undergo direct interactions. That said, given they span 4D in energy, these zero-field split M_S sublevels could approach 100 cm^{-1}, which would put them near coherent vibrational energies that are directly involved in ISC (*vide infra*).[17] Furthermore, there have been reports of magnetic field dependent rates of ISC in Ni(II) complexes.[62,63] Indeed, the model used to interpret these magnetic field dependent ISC rates invoked large values of excited state ZFS (~+24 cm^{-1}).[62] Additionally, different molecular symmetries also gave rise to different magnetic field dependencies on ISC rates, suggesting that different values of ZFSs may manifest in these field dependent rates.[63] Additionally, significant magnetic field effects have been observed on the rates of cooperative SCO for $[Fe(2\text{-pic})_3]Cl_2 \cdot EtOH$ (2-pic = 2-picolylamine).[64] While the authors observed little effect on the transition temperature for SCO (0.2 K), increased magnetic fields dramatically accelerated the rate of formation of the S = 2 state through the LIESST effect (710 % at 7 T relative to 0.5 T).

Additionally, at 10 K, an increased magnetic field dramatically decreased the rate of relaxation to the S = 0 ground state. These combine observations of magnetic field effects on rates of ISC/SCO, together with the observations described in this work, strongly motivate future combined steady state and ultrafast magnetic resonance and optical experiments to measure and quantify variable temperature variable field (VTVH) ISC/SCO kinetics.

3.3. Implications for ISC/SCO and Photophysics. An interesting observation here is that the a_{1g} breathing mode, which has been implicated in ISC/SCO dynamics,[14,16–18] exhibits appreciable linear spin–phonon and excited state coupling terms, demonstrating that the methodology can successfully identify the molecular motions coupled to spin conversion processes. Following the a_{1g} modes in Fe(II) complexes considered here leads directly to ISC and thus provides an opportunity to study the spin–phonon coupling-based mechanism of spin conversion as predicted by CASSCF/NEVPT2 calculations. Indeed, in our preliminary evaluations of spin–phonon coupling terms in $[Fe(bpy)_3]^{2+}$, the a_{1g} breathing mode calculated at ~120 cm^{-1}, which has been identified as the key mode for the ultrafast formation of the $^5T_{2g}$ state,[17] is one of several modes that exhibit appreciable linear spin–phonon coupling terms. These results, as well as a comparison to other photo-active Fe(II) complexes, will be presented in a forthcoming study.

Overall, the model presented here suggests that dynamic ZFSs, which are directly reflected in spin–phonon coupling terms, play a key role and allow for the determination of individual excited state contributions to the ZFS at different positions along a PES. For example, while the ^5E_g states contribute the majority of the ZFS at the equilibrium geometry of $[Fe(H_2O)_6]^{2+}$, at the ISC, the spin-forbidden $^3T_{1g}$ state (and to a small extent the singlets) is the dominant contributor. Concurrently, the $^3T_{1g}$ contribution to the ZFS is a direct reflection of its further role in turning on the $^1A_{1g}$ state mixing with the lowest energy M_S sublevel (Figure 5), consistent with the previously described mechanism of SCO.[56,65–67]

The role of the $^3T_{1g}$ state in the ISC process has been studied in great detail using ultrafast spectroscopies.[68–70] While the triplet state has been identified as a fleeting intermediate during the initial formation of the $^5T_{2g}$ state in Fe(II) polypyridyl compounds,[68,69] we have mainly focused on understanding its role in the direct $^1A_{1g}/^5T_{1g}$ $\Delta S = 2$ spin conversion, which typically governs the overall rate of spin conversion.[60,71] An important finding here is the demonstration that the spin conversion process can be described by quantitatively evaluating the relative intramolecular linear spin–phonon coupling terms for the ^5E_g(1a,1b) and $^3T_{1g}$ states. A future study will focus on

evaluating these ratios across Fe(II) complexes where rates and apparent activation energies can and have been measured using temperature dependent transient absorption spectroscopies.[57,58] These general results can be further extended to the study of spin conversion processes in any S > ½ transition metal complex.

4. Summary.

In summary, we have provided a means to evaluate linear spin–phonon coupling terms in S = 2 Fe(II) complexes, which is useful for identifying modes that are involved in driving ΔS = 2 ISCs in transition metal complexes. Spin–phonon coupling terms originate from the presence of appreciable excited state coupling terms, are sensitive to the initial geometric and electronic structure of the transition metal complex, and will strongly influence ISC dynamics. It is further demonstrated that the CASSCF/NEVPT2 methodology provides a convenient means to describe the mechanism of spin conversion processes and highlights the role of dynamics ZFSs, which manifest in the relative ratios of intramolecular linear excited state coupling terms (Figure 6C and Section 2.4.2) and dominate the mechanism of ISC. Thus, we envision insights from linear spin–phonon and excited state coupling terms can guide the synthetic modification of transition metal complexes for efficient solar energy conversion and photoredox catalysis.

Supplementary Information.

Computational methods, benchmark CASSCF/NEVPT2 calculations, supporting tables and figures, including DFT calculated vibrational modes and fits for linear spin–phonon and excited state coupling terms, Cartesian coordinates of all geometries, and representative ORCA input files.

Acknowledgments.

We acknowledge Dr. Jay Winkler for helpful discussions and Dr. Martin Srnec for assistance with initial CASSCF/NEVPT2 calculations. ATB acknowledges funding through a National Science Foundation Graduate Research Fellowship (NSF Grant No. DGE-1745301). PTK acknowledges funding through the Caltech Summer Undergraduate Research Fellowship (SURF) program. Financial support from Caltech and the Dow Next Generation Educator Fund is gratefully acknowledged.

References

[1] L. Escalera-Moreno, J.J. Baldoví, A. Gaita-Ariño, and E. Coronado, Chem. Sci. **9**, 3265 (2018).
[2] L. Escalera-Moreno, N. Suaud, A. Gaita-Ariño, and E. Coronado, J. Phys. Chem. Lett. **8**, 1695 (2017).
[3] A. Albino, S. Benci, L. Tesi, M. Atzori, R. Torre, S. Sanvito, R. Sessoli, and A. Lunghi, Inorg. Chem. **58**, 10260 (2019).
[4] A. Lunghi, F. Totti, R. Sessoli, and S. Sanvito, Nat. Commun. **8**, 14620 (2017).
[5] A. Lunghi, F. Totti, S. Sanvito, and R. Sessoli, Chem. Sci. **8**, 6051 (2017).
[6] D.H. Moseley, S.E. Stavretis, K. Thirunavukkuarasu, M. Ozerov, Y. Cheng, L.L. Daemen, J. Ludwig, Z. Lu, D. Smirnov, C.M. Brown, A. Pandey, A.J. Ramirez-Cuesta, A.C. Lamb, M. Atanasov, E. Bill, F. Neese, and Z.-L. Xue, Nat. Commun. **9**, 2572 (2018).
[7] M. Atanasov and F. Neese, J. Phys. Conf. Ser. **1148**, 012006 (2018).
[8] R. Mirzoyan and R. Hadt, ChemRxiv. DOI:10.26434/chemrxiv.9985124.v1 (2019).
[9] B. Gu and I. Franco, J. Phys. Chem. Lett. **9**, 773 (2018).
[10] A.J. Fielding, S. Fox, G.L. Millhauser, M. Chattopadhyay, P.M.H. Kroneck, G. Fritz, G.R. Eaton, and S.S. Eaton, J. Magn. Reson. **179**, 92 (2006).
[11] R. Orbach, Proc. Phys. Soc. **77**, 821 (1961).
[12] K.N. Shrivastava, Phys. Status Solidi B **117**, 437 (1983).
[13] J.H. Van Vleck, Phys. Rev. **57**, 426 (1940).
[14] C. Bressler, C. Milne, V.-T. Pham, A. ElNahhas, R.M. van der Veen, W. Gawelda, S. Johnson, P. Beaud, D. Grolimund, M. Kaiser, C.N. Borca, G. Ingold, R. Abela, and M. Chergui, Science **323**, 489 (2009).
[15] M. Chergui and E. Collet, Chem. Rev. **117**, 11025 (2017).
[16] M. Cammarata, R. Bertoni, M. Lorenc, H. Cailleau, S. Di Matteo, C. Mauriac, S.F. Matar, H. Lemke, M. Chollet, S. Ravy, C. Laulhé, J.-F. Létard, and E. Collet, Phys. Rev. Lett. **113**, 227402 (2014).
[17] H.T. Lemke, K.S. Kjær, R. Hartsock, T.B. van Driel, M. Chollet, J.M. Glownia, S. Song, D. Zhu, E. Pace, S.F. Matar, M.M. Nielsen, M. Benfatto, K.J. Gaffney, E. Collet, and M. Cammarata, Nat. Commun. **8**, 15342 (2017).
[18] A. Marino, M. Cammarata, S.F. Matar, J.-F. Létard, G. Chastanet, M. Chollet, J.M. Glownia, H.T. Lemke, and E. Collet, Struct. Dyn. **3**, 023605 (2015).
[19] K. Kunnus, M. Vacher, T.C.B. Harlang, K.S. Kjær, K. Haldrup, E. Biasin, T.B. van Driel, M. Pápai, P. Chabera, Y. Liu, H. Tatsuno, C. Timm, E. Källman, M. Delcey, R.W. Hartsock, M.E. Reinhard, S. Koroidov, M.G. Laursen, F.B. Hansen, P. Vester, M. Christensen, L. Sandberg, Z. Németh, D.S. Szemes, É. Bajnóczi, R. Alonso-Mori, J.M. Glownia, S. Nelson, M. Sikorski, D. Sokaras, H.T. Lemke, S.E. Canton, K.B. Møller, M.M. Nielsen, G. Vankó, K. Wärnmark, V. Sundström, P. Persson, M. Lundberg, J. Uhlig, and K.J. Gaffney, Nat. Commun. **11**, 1 (2020).
[20] K.S. Kjær, T.B.V. Driel, T.C.B. Harlang, K. Kunnus, E. Biasin, K. Ledbetter, R.W. Hartsock, M.E. Reinhard, S. Koroidov, L. Li, M.G. Laursen, F.B. Hansen, P. Vester, M. Christensen, K. Haldrup, M.M. Nielsen, A.O. Dohn, M.I. Pápai, K.B. Møller, P. Chabera, Y. Liu, H. Tatsuno, C. Timm, M. Jarenmark, J. Uhlig, V. Sundstöm, K. Wärnmark, P. Persson, Z. Németh, D.S. Szemes, É. Bajnóczi, G. Vankó, R. Alonso-Mori, J.M. Glownia, S. Nelson, M. Sikorski, D. Sokaras, S.E. Canton, H.T. Lemke, and K.J. Gaffney, Chem. Sci. **10**, 5749 (2019).

[21] H. Tatsuno, K.S. Kjær, K. Kunnus, T.C.B. Harlang, C. Timm, M. Guo, P. Chàbera, L.A. Fredin, R.W. Hartsock, M.E. Reinhard, S. Koroidov, L. Li, A.A. Cordones, O. Gordivska, O. Prakash, Y. Liu, M.G. Laursen, E. Biasin, F.B. Hansen, P. Vester, M. Christensen, K. Haldrup, Z. Németh, D.S. Szemes, É. Bajnóczi, G. Vankó, T.B.V. Driel, R. Alonso-Mori, J.M. Glownia, S. Nelson, M. Sikorski, H.T. Lemke, D. Sokaras, S.E. Canton, A.O. Dohn, K.B. Møller, M.M. Nielsen, K.J. Gaffney, K. Wärnmark, V. Sundström, P. Persson, and J. Uhlig, Angew. Chem. Int. Ed. **59**, 364 (2020).
[22] D.M. Arias-Rotondo and J.K. McCusker, Chem. Soc. Rev. **45**, 5803 (2016).
[23] J.D. Braun, I.B. Lozada, C. Kolodziej, C. Burda, K.M.E. Newman, J. van Lierop, R.L. Davis, and D.E. Herbert, Nat. Chem. **11**, 1144 (2019).
[24] K.S. Kjær, N. Kaul, O. Prakash, P. Chábera, N.W. Rosemann, A. Honarfar, O. Gordivska, L.A. Fredin, K.-E. Bergquist, L. Häggström, T. Ericsson, L. Lindh, A. Yartsev, S. Styring, P. Huang, J. Uhlig, J. Bendix, D. Strand, V. Sundström, P. Persson, R. Lomoth, and K. Wärnmark, Science **363**, 249 (2019).
[25] J.K. McCusker, Science **363**, 484 (2019).
[26] J.C. Deaton, M.S. Gebhard, S.A. Koch, Michelle. Millar, and E.I. Solomon, J. Am. Chem. Soc. **110**, 6241 (1988).
[27] F. Neese and E.I. Solomon, Inorg. Chem. **37**, 6568 (1998).
[28] R. Boča, Coord. Chem. Rev. **248**, 757 (2004).
[29] A. Lunghi, ArXiv191204545 Cond-Mat Physicsquant-Ph (2019).
[30] M. S. Fataftah, M. D. Krzyaniak, B. Vlaisavljevich, M. R. Wasielewski, J. M. Zadrozny, and D. E. Freedman, Chem. Sci. (2019).
[31] E.I. Solomon, E.G. Pavel, K.E. Loeb, and C. Campochiaro, Coord. Chem. Rev. **144**, 369 (1995).
[32] C. Corliss and J. Sugar, J. Phys. Chem. Ref. Data **11**, 135 (1982).
[33] V. P. Gnezdilov, V. V. Eremenko, A. V. Peschanskii, and V. I. Fomin, Fiz. Nizk. Tem. **17**, 253 (1953).
[34] E.I. Solomon, Comments Inorg. Chem. **3**, 227 (1984).
[35] E.A. Suturina, D. Maganas, E. Bill, M. Atanasov, and F. Neese, Inorg. Chem. **54**, 9948 (2015).
[36] M. Atanasov, D. Aravena, E. Suturina, E. Bill, D. Maganas, and F. Neese, Coord. Chem. Rev. **289–290**, 177 (2015).
[37] M. Atanasov, D. Ganyushin, D.A. Pantazis, K. Sivalingam, and F. Neese, Inorg. Chem. **50**, 7460 (2011).
[38] C. Sousa and C. de Graaf, in *Spin States Biochem. Inorg. Chem.* (Wiley-Blackwell, 2015), pp. 35–57.
[39] C. Sousa, A. Domingo, and C. de Graaf, Chem. – Eur. J. **24**, 5146 (2018).
[40] C. Sousa, C. de Graaf, A. Rudavskyi, R. Broer, J. Tatchen, M. Etinski, and C.M. Marian, Chem. – Eur. J. **19**, 17541 (2013).
[41] C. Sousa, C. de Graaf, A. Rudavskyi, and R. Broer, J. Phys. Chem. A **121**, 9720 (2017).
[42] A. Rudavskyi, C. Sousa, C. de Graaf, R.W.A. Havenith, and R. Broer, J. Chem. Phys. **140**, 184318 (2014).
[43] L.C. Jackson, Philos. Mag. J. Theor. Exp. Appl. Phys. **4**, 269 (1959).
[44] P.M. Champion and A.J. Sievers, J. Chem. Phys. **66**, 1819 (1977).
[45] R.S. Rubins and H.R. Fetterman, J. Chem. Phys. **71**, 5163 (1979).
[46] G. Agnetta, T. Garofano, M.B. Palma-Vittorelli, and M.U. Palma, Philos. Mag. J. Theor. Exp. Appl. Phys. **7**, 495 (1962).

[47] C. Campochiaro, E.G. Pavel, and E.I. Solomon, Inorg. Chem. **34**, 4669 (1995).
[48] W.C. Hamilton, Acta Crystallogr. **15**, 353 (1962).
[49] F. Neese, Wiley Interdiscip. Rev. Comput. Mol. Sci. **2**, 73 (2012).
[50] F. Neese, Wiley Interdiscip. Rev. Comput. Mol. Sci. **8**, e1327 (2018).
[51] E. Roedern and T.R. Jensen, Inorg. Chem. **54**, 10477 (2015).
[52] R. Eßmann, G. Kreiner, A. Niemann, D. Rechenbach, A. Schmieding, T. Sichla, U. Zachwieja, and H. Jacobs, Z. Für Anorg. Allg. Chem. **622**, 1161 (1996).
[53] H. Jacobs, J. Bock, and C. Stüve, J. Common Met. **134**, 207 (1987).
[54] L. McGhee, R.M. Siddique, and J.M. Winfield, J. Chem. Soc. Dalton Trans. 1309 (1988).
[55] R.B. Wilson and E.I. Solomon, J. Am. Chem. Soc. **102**, 4085 (1980).
[56] E. Buhks, G. Navon, M. Bixon, and J. Jortner, J. Am. Chem. Soc. **102**, 2918 (1980).
[57] C.L. Xie and D.N. Hendrickson, J. Am. Chem. Soc. **109**, 6981 (1987).
[58] J.K. McCusker, A.L. Rheingold, and D.N. Hendrickson, Inorg. Chem. **35**, 2100 (1996).
[59] K.F. Purcell, J. Am. Chem. Soc. **101**, 5147 (1979).
[60] E. König, in *Complex Chem.* (Springer Berlin Heidelberg, 1991), pp. 51–152.
[61] J.K. McCusker, H. Toftlund, A.L. Rheingold, and D.N. Hendrickson, J. Am. Chem. Soc. **115**, 1797 (1993).
[62] C. Musewald, P. Gilch, G. Hartwich, F. Pöllinger-Dammer, H. Scheer, and M.E. Michel-Beyerle, J. Am. Chem. Soc. **121**, 8876 (1999).
[63] P. Gilch, C. Musewald, and M.E. Michel-Beyerle, Chem. Phys. Lett. **325**, 39 (2000).
[64] Y. Ogawa, T. Ishikawa, S. Koshihara, K. Boukheddaden, and F. Varret, Phys. Rev. B **66**, 073104 (2002).
[65] A. Hauser, Coord. Chem. Rev. **111**, 275 (1991).
[66] A. Hauser, A. Vef, and P. Adler, J. Chem. Phys. **95**, 8710 (1991).
[67] S. Schenker, A. Hauser, W. Wang, and I.Y. Chan, J. Chem. Phys. **109**, 9870 (1998).
[68] W. Zhang, R. Alonso-Mori, U. Bergmann, C. Bressler, M. Chollet, A. Galler, W. Gawelda, R.G. Hadt, R.W. Hartsock, T. Kroll, K.S. Kjær, K. Kubiček, H.T. Lemke, H.W. Liang, D.A. Meyer, M.M. Nielsen, C. Purser, J.S. Robinson, E.I. Solomon, Z. Sun, D. Sokaras, T.B. van Driel, G. Vankó, T.-C. Weng, D. Zhu, and K.J. Gaffney, Nature **509**, 345 (2014).
[69] K. Zhang, R. Ash, G.S. Girolami, and J. Vura-Weis, J. Am. Chem. Soc. **141**, 17180 (2019).
[70] G. Auböck and M. Chergui, Nat. Chem. **7**, 629 (2015).
[71] M. Bacci, Coord. Chem. Rev. **86**, 245 (1988).

Supporting Information

Spin–Phonon Coupling and Dynamic Zero Field Splitting Contributions to Spin Conversion Processes in Iron(II) Complexes

Nicholas J. Higdon, Alexandra T. Barth, Patryk T. Kozlowski, and Ryan G. Hadt*

Division of Chemistry and Chemical Engineering, Arthur Amos Noyes Laboratory of Chemical Physics, California Institute of Technology, Pasadena, California, 91125, United States

Corresponding Author: rghadt@caltech.edu

Table of Contents

A. Computational Methods

All calculations were carried out using ORCA[1,2], version 4.2.0 on the High Performance Computing Cluster at Caltech. Representative input parameters for density functional theory (DFT) based optimization and frequency calculations, as well as subsequent complete active space self-consistent field (CASSCF), N-electron valence state perturbation theory (NEVPT2) calculations are provided in the "Representative Orca Input Files" section of this document. For all complexes, DFT calculations were carried out with a BP86[3–5] exchange correlation functional. All calculations were carried out using the def2-TZVP[6] basis set with auxiliary basis set def2/J on all ligating atoms. DFT grid 7 and tight SCF convergence criteria corresponding to a convergence tolerance of 10^{-8} Hartrees were used for all DFT calculations.

CASSCF and subsequent NEVPT2[7–11] calculations were used to account for relativistic effects. Single point energy calculations were carried out using def2-TZVP basis set and PAtom initial guess molecular orbitals. For Fe(II) d^6, the active space consists of five orbitals corresponding to the Fe 3d orbitals. For the ^5D term symbol, there are one hundred possible states to include in the CASSCF/NEVPT2 calculation. To limit the number of states required for each calculation, the number of roots, 5 quintets, 17 triplets, and 5 singlets and were chosen for all CASSCF-NEVPT2 calculations. Comparisons to calculations using the maximum number of states (i.e., 5 quintets, 45 triplets, and 50 singlets) are included in Table S1 to justify this selection. For select calculations, an expanded active space comprised of the five Fe 3d orbitals and the two ligand/Fe 3d-based σ bonding orbitals (with respect to $d(x^2-y^2)$ and $d(z^2)$ were used to validate the use of the minimum active space (Table S1).

The calculated normal modes q_k are presented in ORCA as cartesian displacements weighted by the diagonal matrix $M(i,i) = \frac{1}{\sqrt{m[i]}}$, where $m[i]$ is the mass of the displaced atom.

$$Q = \sum_i c_i q_i$$

$$q_i = \sqrt{m}_i x_i$$

If Q is normalized to 1, then the reduced mass is related by the following:

$$\mu = \frac{1}{\sum_i \frac{{c_i}^2}{m_i}}$$

Which is then related to the harmonic angular frequency ω and harmonic force constant k through $\omega^2 = k/\mu$.

Displacement along normal modes is done by multiplying the displacement vector q_i by a distortion scaling factor n, such that the displaced vector is defined by nq_i. All spin-phonon coupling calculations presented here were performed between n = -0.01 and n = 0.01 in 7 increments to obtain coupling terms that are reflective of the equilibrium geometry.

B. Tables

Table S1. CASSCF/NEVPT2 calculations testing the size of the active space and number of states for determining the zero field splitting parameter, D, and the energies of the lowest M_S sublevels (ES1 – ES4). The experimental values are given in Figure 1 of the main text.

Structure	Active Space (e^-, Orbital)	States (Q , T, S)	D[c]	ES 1[c]	ES 2[c]	ES 3[c]	ES 4[c]
$[Fe(H_2O)_6]^{2+}$ exp[a]	6, 5	3, 0, 0	5.6	5.5	5.5	22.4	22.4
		5, 0, 0	7.4	7.3	7.3	29.5	29.5
		5, 0, 1	7.4	7.3	7.3	29.7	29.7
		5, 0, 15	7.2	7.1	7.1	28.6	28.6
		5, 1, 0	9.2	9.1	9.1	36.8	36.8
		5, 3, 0	8.6	8.5	8.5	34.2	34.2
		5, 6, 0	8.3	8.2	8.2	33.2	33.2
		5, 1, 1	9.5	9.4	9.4	37.8	37.8
		5, 17, 15	**9.6**	**9.6**	**9.6**	**38.6**	**38.6**
		5, 45, 50	**9.4**	**9.4**	**9.4**	**37.7**	**37.7**
	10, 7	**5, 17, 15**	**9.7**	**9.7**	**9.7**	**38.9**	**38.9**
		5, 45, 50	**9.5**	**9.5**	**9.5**	**38.0**	**38.0**
$[Fe(H_2O)_6]^{2+}$[b]	6, 5	3, 0, 0	19.8	10.4	23.4	78.2	79.4
		5, 0, 0	19.6	8.0	27.7	78.0	80.8
		5, 0, 1	19.9	8.3	27.8	79.2	81.9
		5, 0, 15	18.8	7.8	27.1	75.1	77.8
		5, 1, 0	17.1	4.7	29.6	69.5	73.9
		5, 3, 0	19.2	7.0	29.7	77.0	80.5
		5, 6, 0	18.8	6.7	29.3	75.3	78.8
		5, 1, 1	17.9	5.6	29.1	72.3	76.0
		5, 17, 15	**18.3**	**6.0**	**30.3**	**73.6**	**77.7**
		5, 45, 50	**19.3**	**6.6**	**31.0**	**77.5**	**81.5**
	10, 7	**5, 17, 15**	**18.1**	**5.9**	**30.3**	**73.0**	**77.1**
		5, 45, 50	**19.2**	**6.5**	**31.0**	**76.9**	**81.0**

[a] Neutron diffraction structure; [b] BP86 optimized structure; [c] cm^{-1}

Calculations utilizing either 6, 5 or 10, 7 active spaces with 5 quintets, 17 triplets, and 15 singlets or 5 quintets, 45 triplets, and 50 singlets provide similar overall ZFS parameters. Thus, we have employed the 6, 5 active space with 5 quintets, 17 triplets, and 15 singlets for all calculations in this research unless otherwise specified.

Table S2. DFT calculated vibrational modes for the neutron diffraction structure of $[Fe(H_2O)_6]^{2+}$, including their energies, mode classifications, symmetry labels, and scaled vector displacements. Note only the main vibrations given in Figure 2 of the main text are formally assigned symmetry labels.

Mode	Energy / cm^{-1}	Type	Symmetry	Scaled Vector Displacements
1	-1691.14	Ligand Based	-	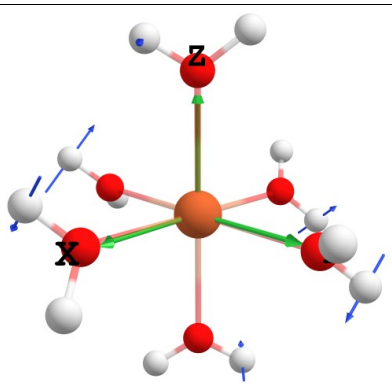
2	-1689.06	Ligand Based	-	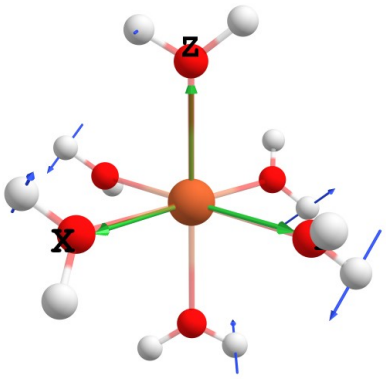
3	-1648.39	Ligand Based	-	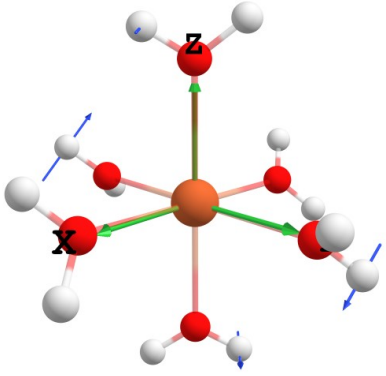

4	-1648.23	Ligand Based	-	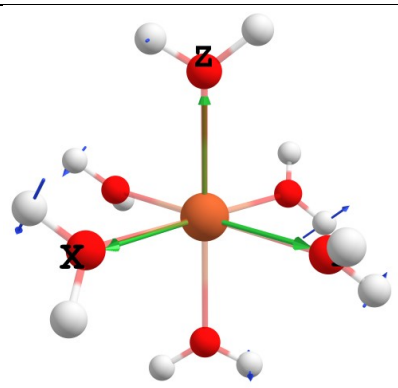
5	-1645.45	Ligand Based	-	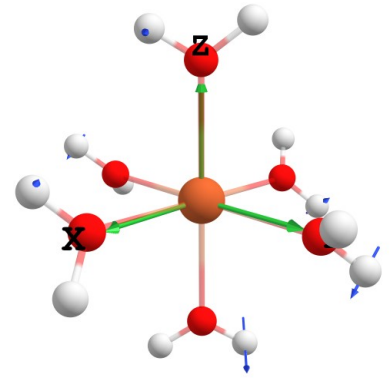
6	-1645.41	Ligand Based	-	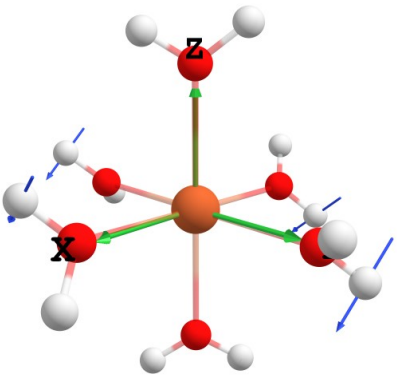
7	-1335.5	Ligand Twisting	-	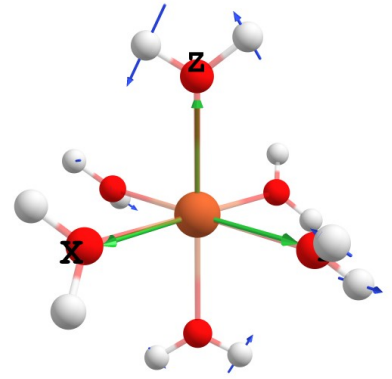

8	-1335.37	Ligand Twisting	-	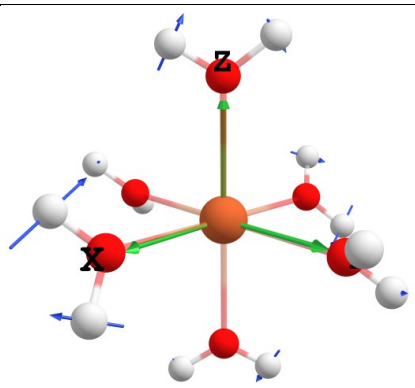
9	-1333.93	Ligand Twisting	-	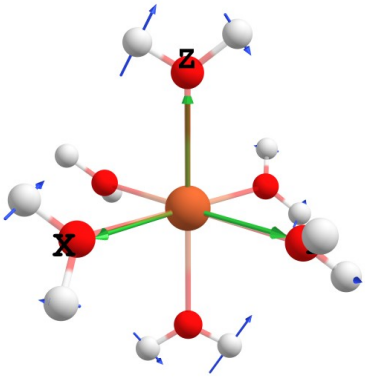
10	-1333.88	Ligand Twisting	-	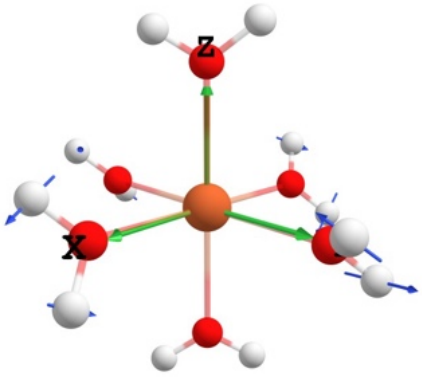
11	-1288.73	Ligand Twisting	-	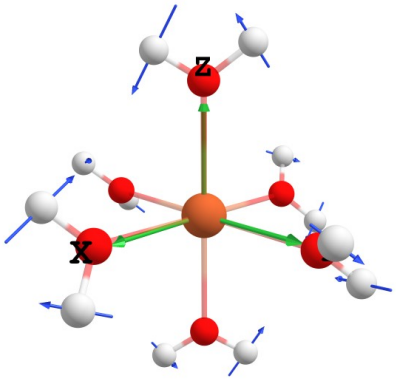

12	-1286.28	Ligand Twisting	-	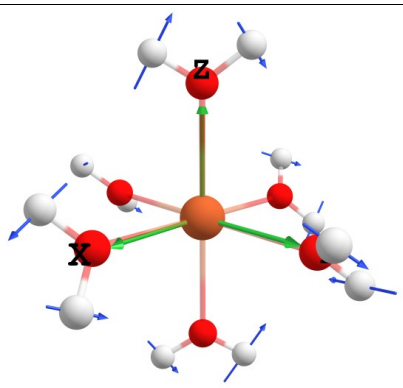
13	-996.26	Ligand Based	-	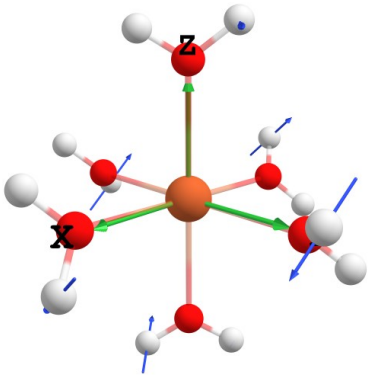
14	-976.33	Ligand Based	-	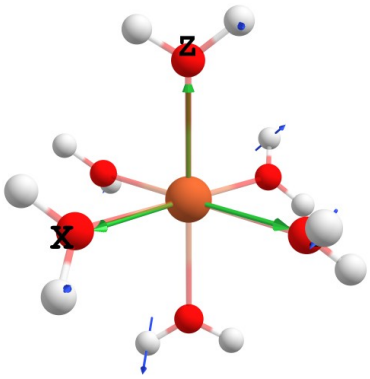
15	-976.22	Ligand Based	-	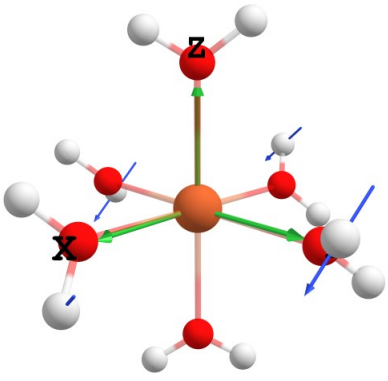

16	-963.14	Ligand Based	-	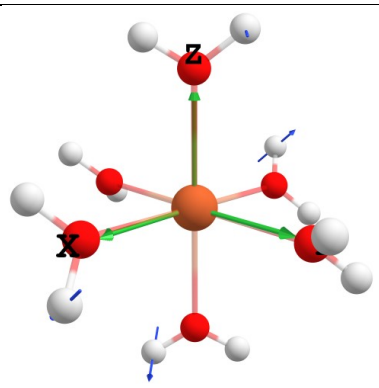
17	-963.02	Ligand Based	-	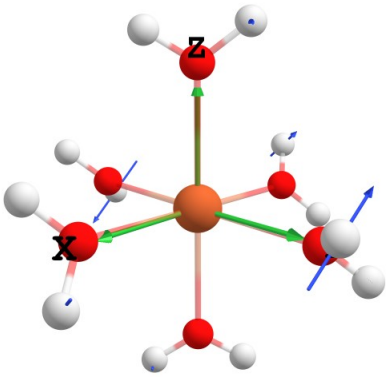
18	-942.81	Ligand Based	-	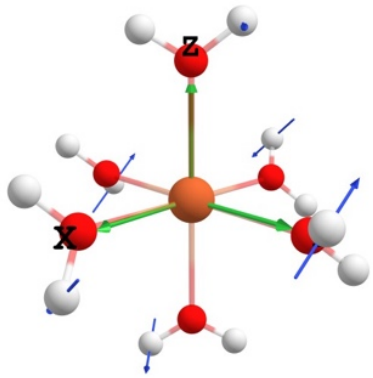
19	54.2	Ligand Metal Bending Ungerade	-	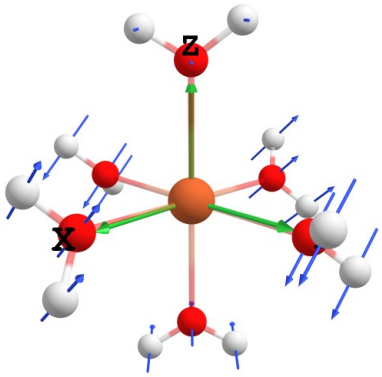

20	117.4	Ligand Metal Bending Ungerade	-	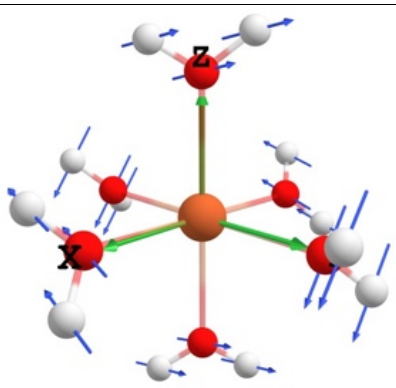
21	117.44	Ligand Metal Bending Ungerade	-	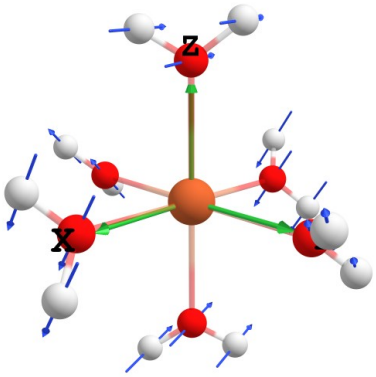
22	134.82	Ligand Metal Bending Gerade	t_{2g}	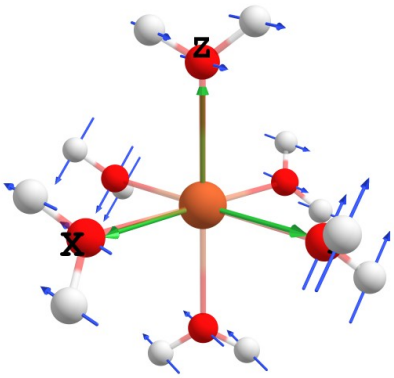
23	134.83	Ligand Metal Bending Gerade	t_{2g}	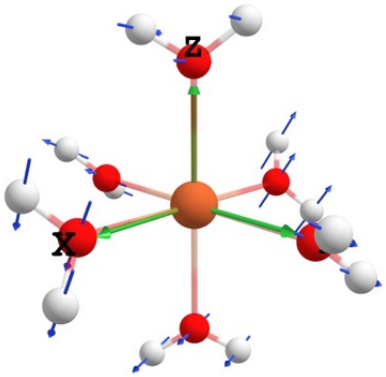

24	170.38	Ligand Metal Bending Ungerade	-	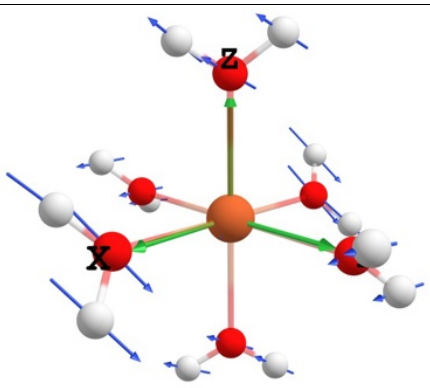
25	170.43	Ligand Metal Bending Ungerade	-	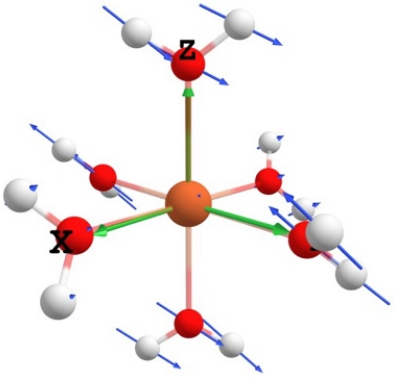
26	181.11	Ligand Metal Bending Gerade	t_{2g}	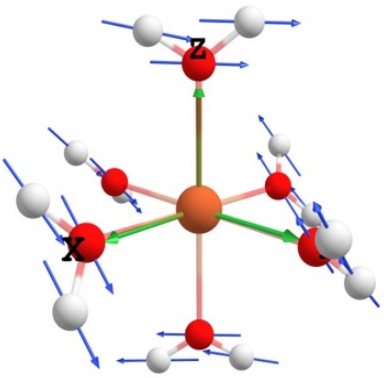
27	217.05	Ligand Metal Bending Ungerade	-	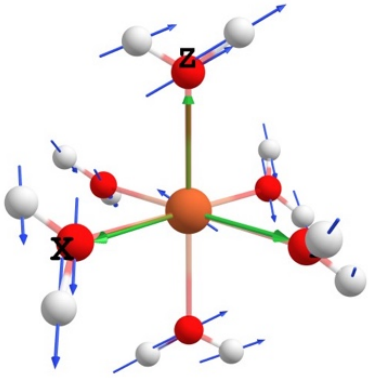

28	244.13	Ligand Metal Stretching Gerade	$e_g\,(\varepsilon)$	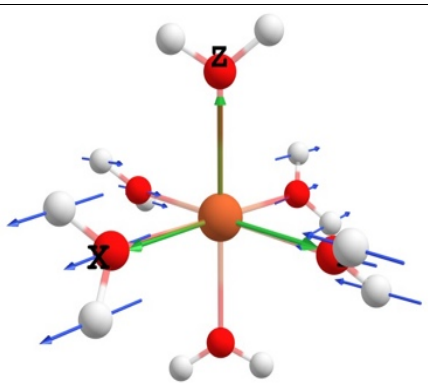
29	244.16	Ligand Metal Stretching Gerade	$e_g\,(\theta)$	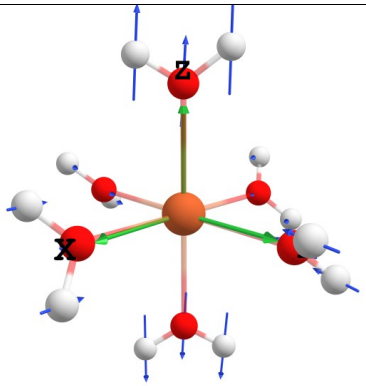
30	333.54	Ligand Metal Stretching Ungerade	t_{1u}	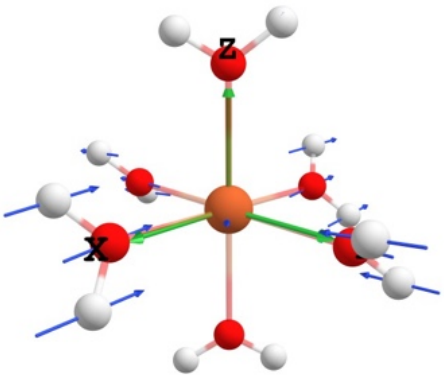
31	333.57	Ligand Metal Stretching Ungerade	t_{1u}	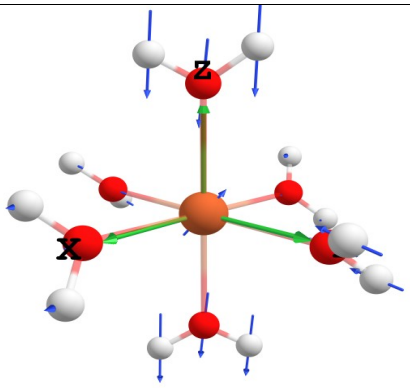

32	340.62	Ligand Metal Stretching Gerade	t_{1g}	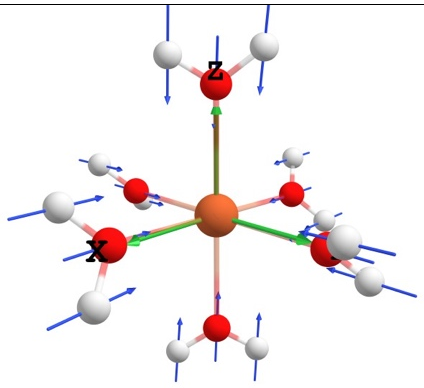
33	341.42	Ligand Metal Stretching Ungerade	t_{1u}	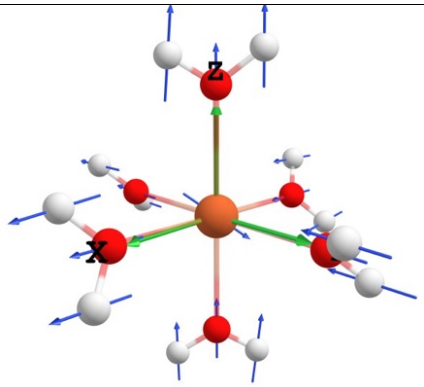
34	1154.18	Ligand Based	-	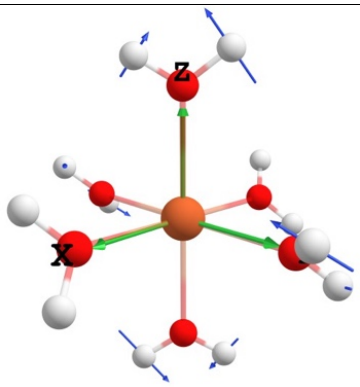
35	1154.27	Ligand Based	-	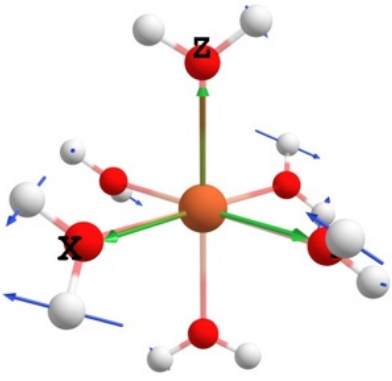

36	1157.62	Ligand Based	-	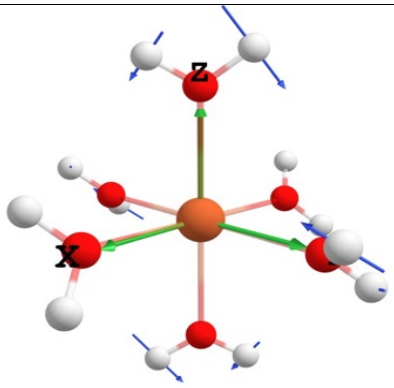
37	1157.69	Ligand Based	-	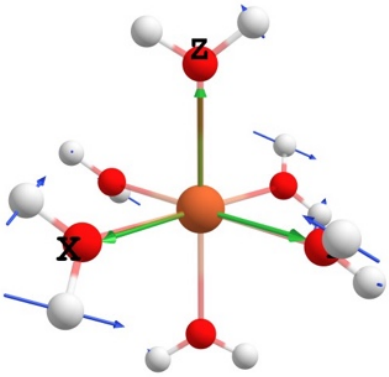
38	1168.52	Ligand Based	-	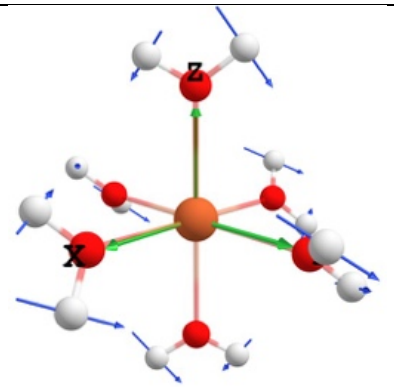
39	1182.68	Ligand Based	-	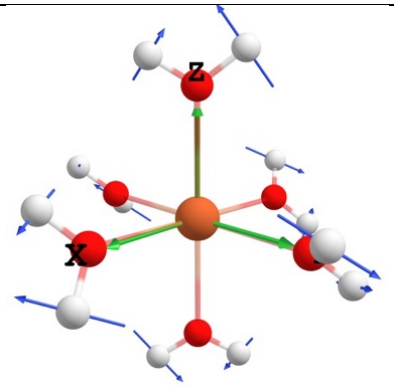

40	4484.85	Ligand Based	-	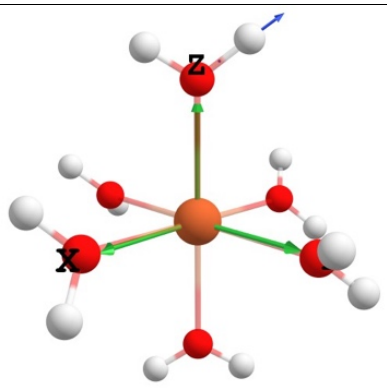
41	4485.24	Ligand Based	-	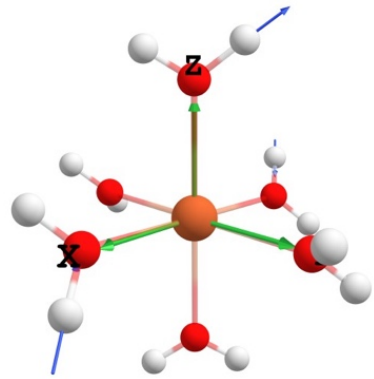
42	4485.86	Ligand Based	-	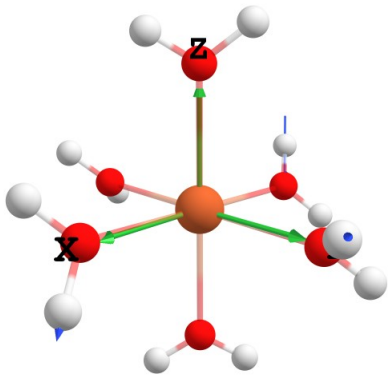
43	4486.32	Ligand Based	-	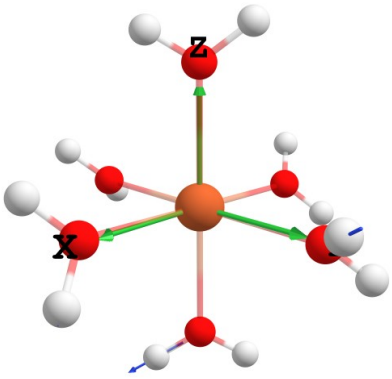

44	4486.66	Ligand Based	-	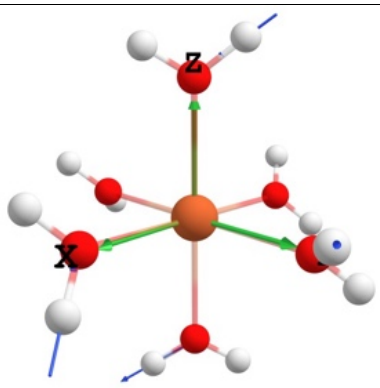
45	4490.01	Ligand Based	-	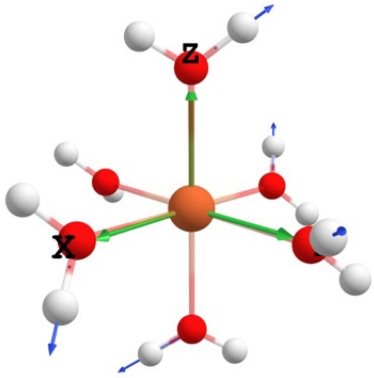
46	5475.29	Ligand Based	-	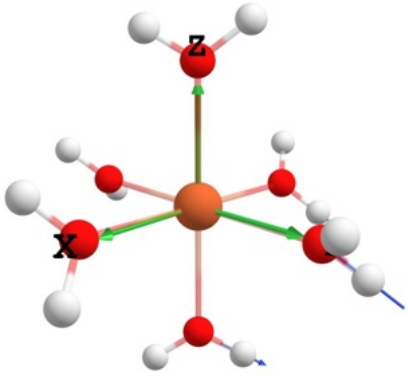
47	5475.67	Ligand Based	-	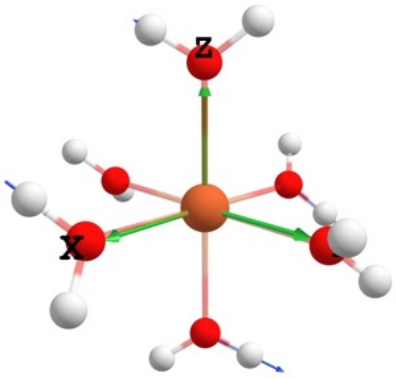

48	5476.3	Ligand Based	-	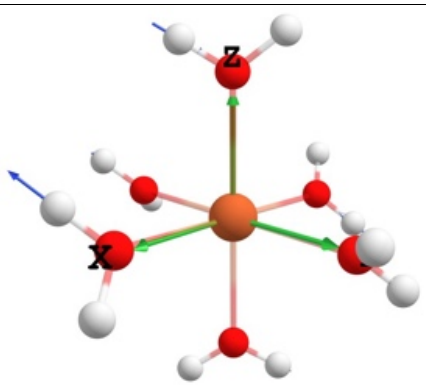
49	5476.92	Ligand Based	-	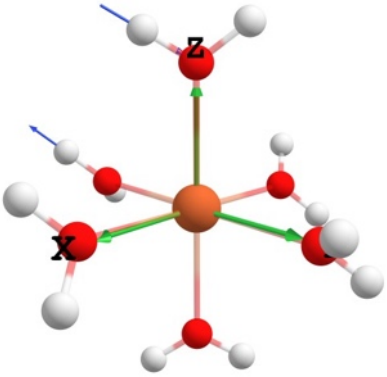
50	5481.2	Ligand Based	-	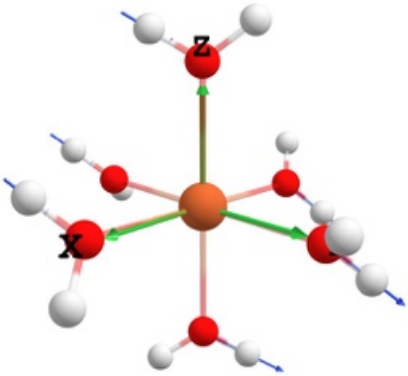
51	5483.44	Ligand Based	-	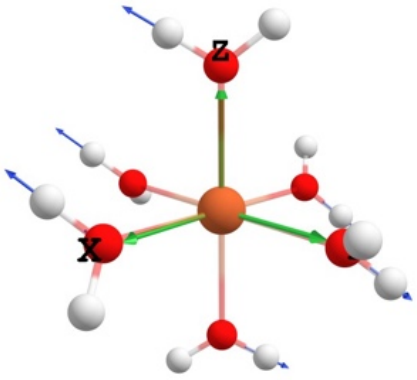

Table S3. DFT calculated vibrational modes for BP86 optimized $[Fe(H_2O)_6]^{2+}$, including their energies, mode classifications, symmetry labels, and scaled vector displacements. Note only the main vibrations given in Figure 2 of the main text are formally assigned symmetry labels.

Mode	Energy / cm^{-1}	Type	Symmetry	Scaled Vector Displacements
1	63.88	Ligand-Metal Bending Gerade	t_{2g}	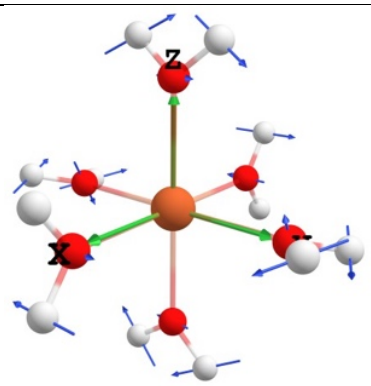
2	72.99	Ligand-Metal Bending Ungerade	-	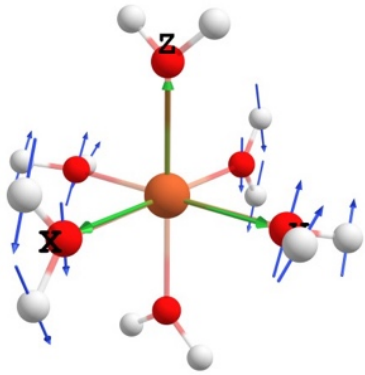
3	79.01	Ligand-Metal Bending Ungerade	-	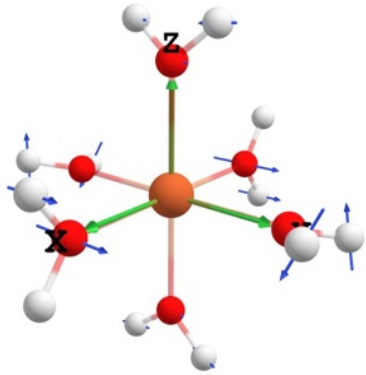

4	80.85	Ligand-Metal Bending Gerade	t_{2g}	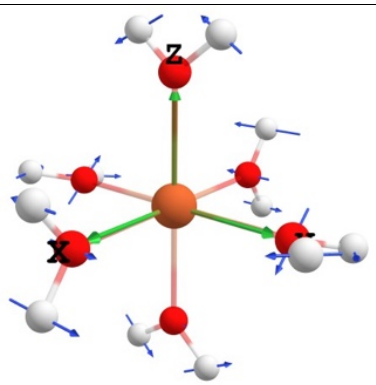
5	85.79	Ligand-Metal Bending Ungerade	-	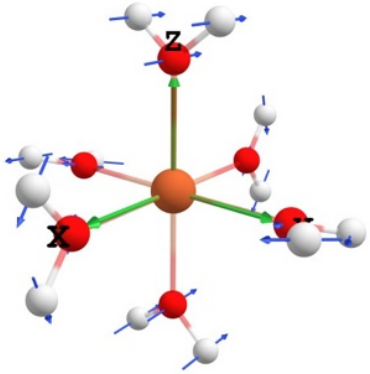
6	94.01	Ligand Twisting	-	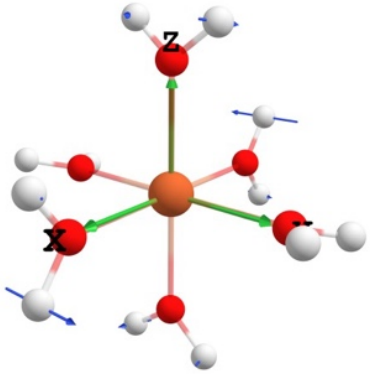
7	105.6	Ligand-Metal Bending Gerade	t_{2g}	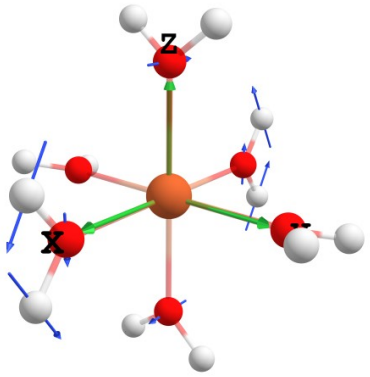

8	106.24	Ligand-Metal Bending Ungerade	-	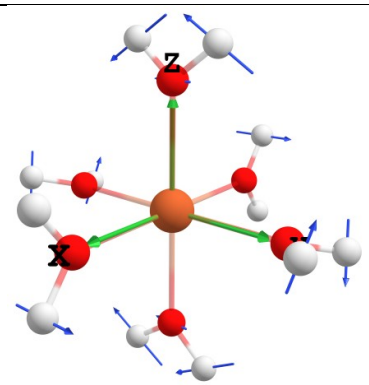
9	129.13	Ligand-Metal Bending Ungerade	-	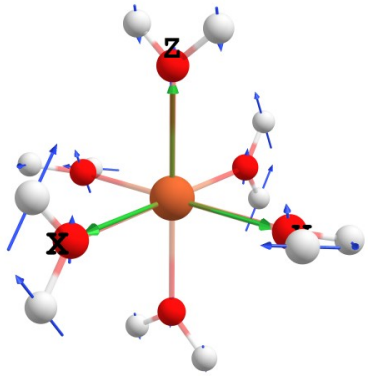
10	138.63	Ligand-Metal Bending Ungerade	-	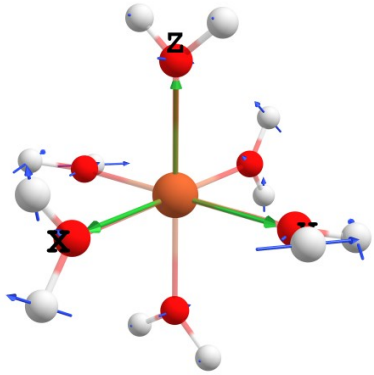
11	170.62	Ligand-Metal Stretching Gerade	e_g (ε)	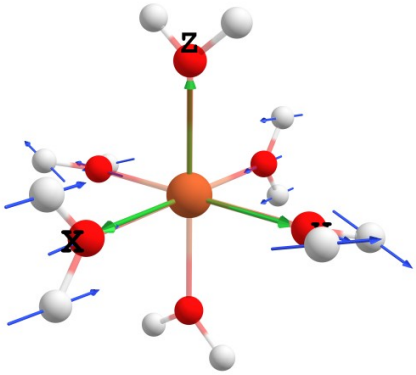

12	179.06	Ligand Twisting	-	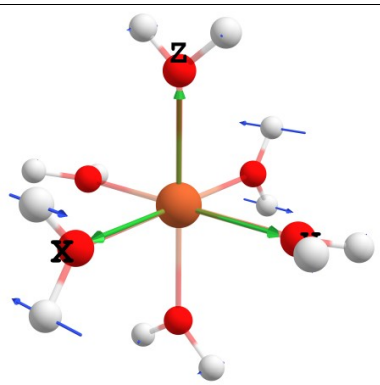
13	227.31	Ligand-Metal Stretching Gerade	$e_g(\theta)$	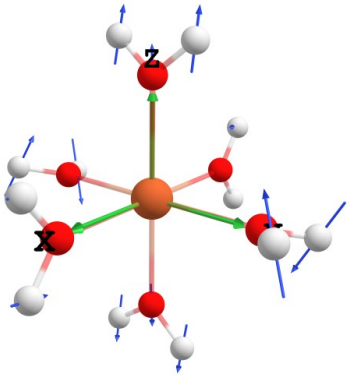
14	234.35	Ligand Twisting	-	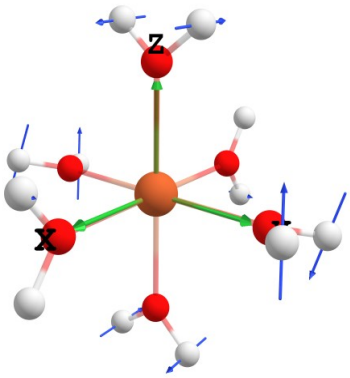
15	260.87	Ligand Twisting	-	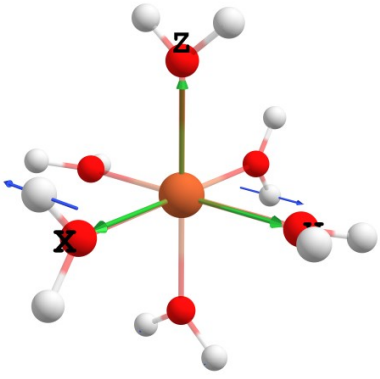

16	273	Ligand Twisting	-	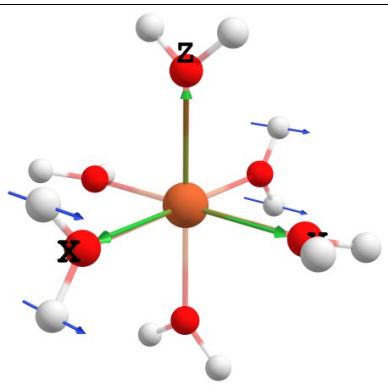
17	273.82	Ligand Twisting	-	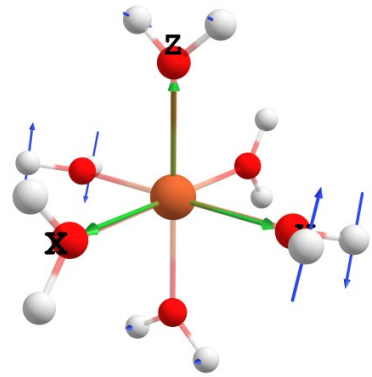
18	295.53	Ligand-Metal Stretching Ungerade	t_{1u}	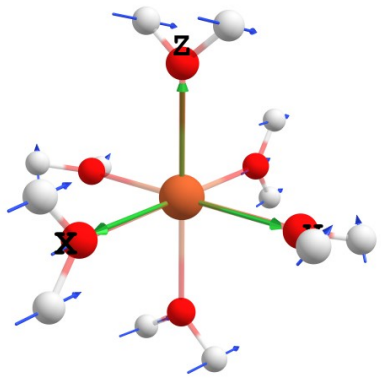
19	299.86	Ligand-Metal Stretching Ungerade	t_{1u}	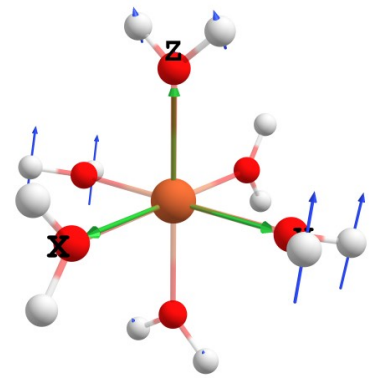

20	309.74	Ligand Twisting	-	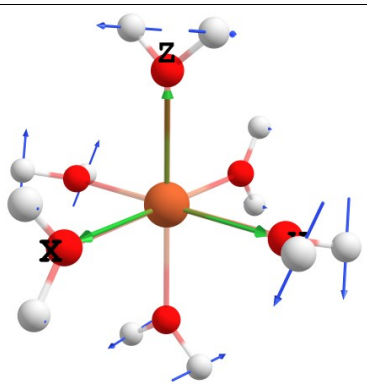
21	323.31	Ligand-Metal Stretching Gerade	a_{1g}	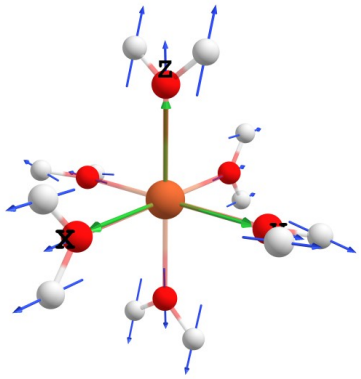
22	334.85	Ligand Twisting	-	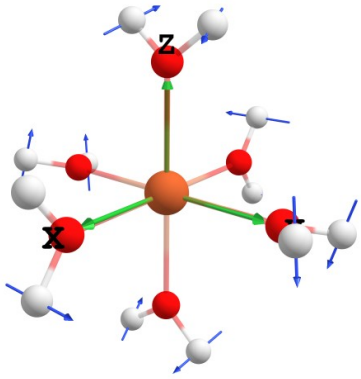
23	336.61	Ligand-Metal Stretching Ungerade	t_{1u}	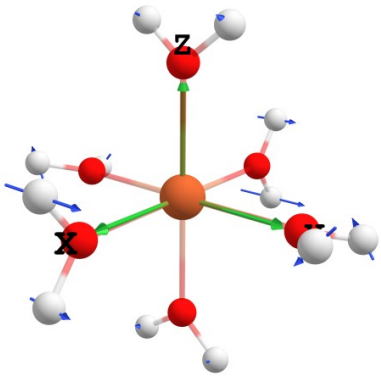

24	346.38	Ligand Twisting	-	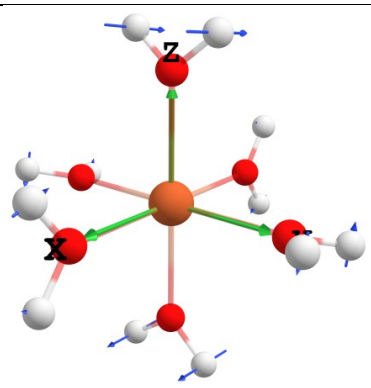
25	347.46	Ligand Twisting	-	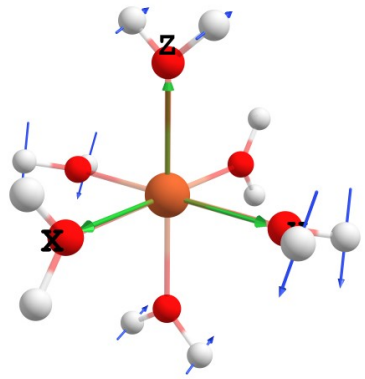
26	372.31	Ligand Twisting	-	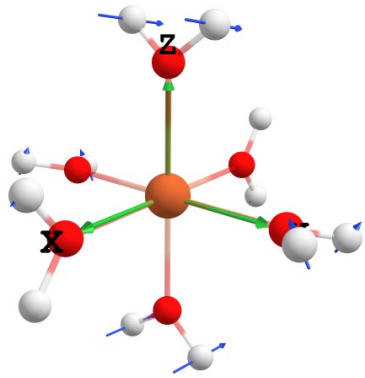
27	404.75	Ligand Twisting	-	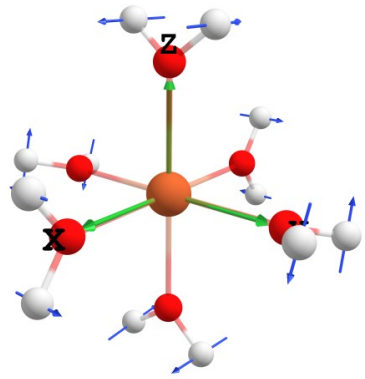

28	482.99	Ligand Twisting	-	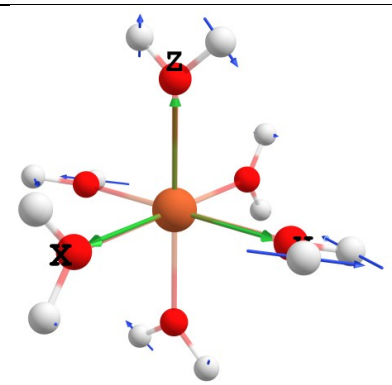
29	503.06	Ligand Twisting	-	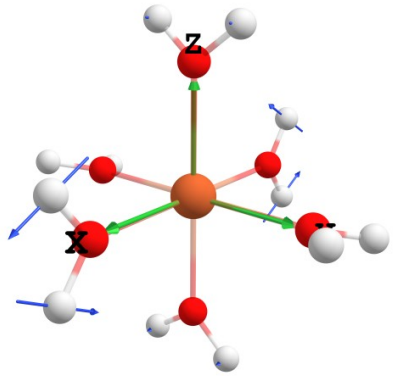
30	505.64	Ligand Twisting	-	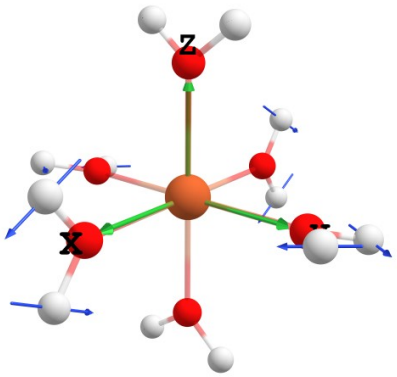
31	511.04	Ligand Twisting	-	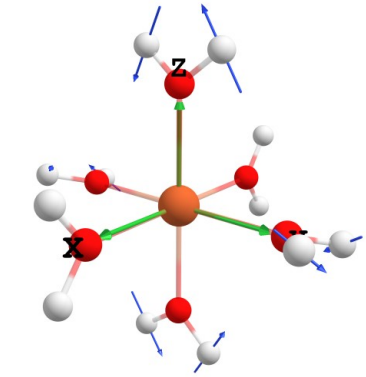

32	529.33	Ligand Twisting	-	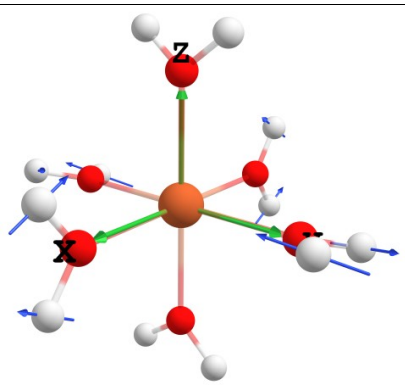
33	535.82	Ligand Twisting	-	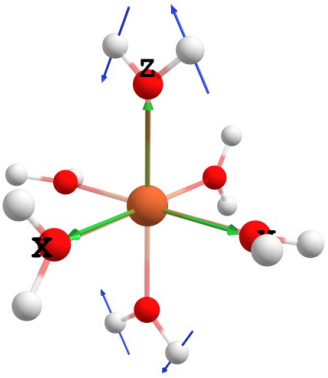
34	1597.01	Ligand Based	-	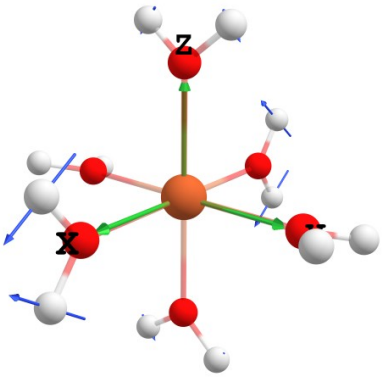
35	1597.11	Ligand Based	-	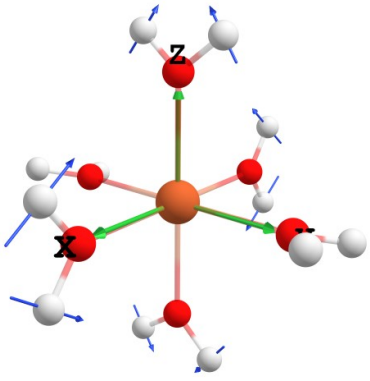

36	1598.88	Ligand Based	-	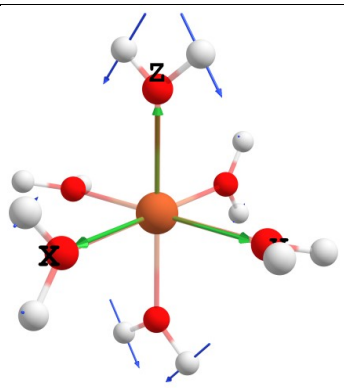
37	1599.49	Ligand Based	-	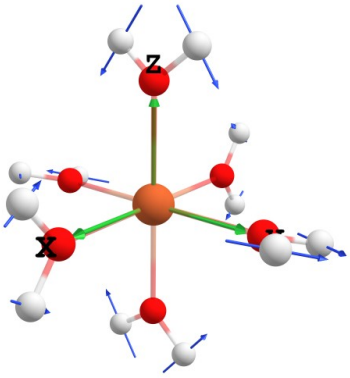
38	1603.03	Ligand Based	-	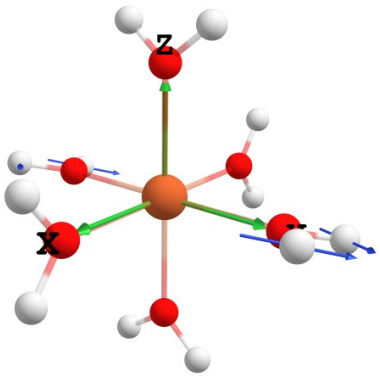
39	1610.47	Ligand Based	-	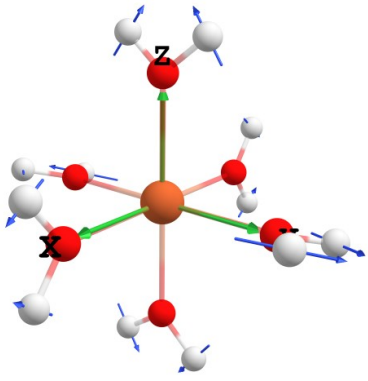

40	3634.59	Ligand Based	-	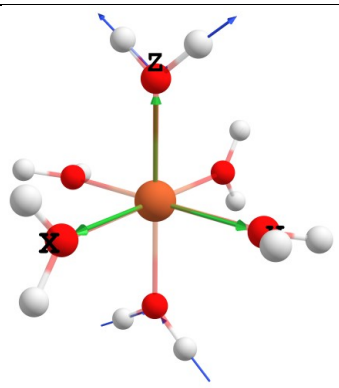
41	3635.48	Ligand Based	-	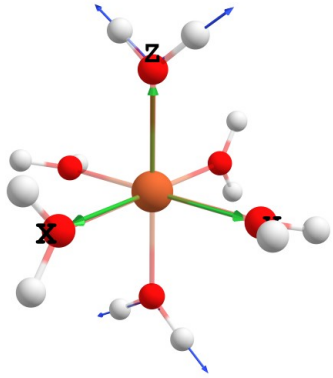
42	3640.97	Ligand Based	-	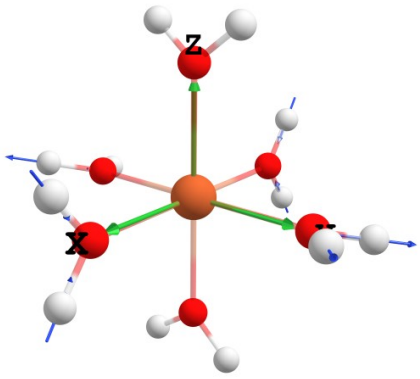
43	3644	Ligand Based	-	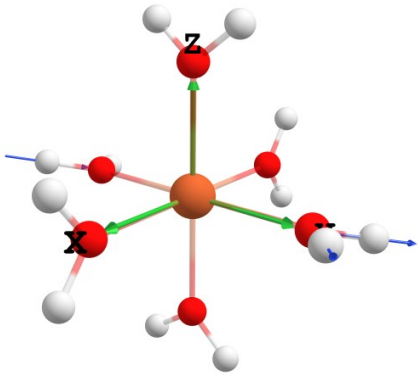

44	3646.86	Ligand Based	-	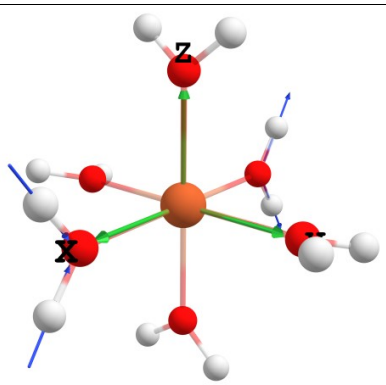
45	3649.13	Ligand Based	-	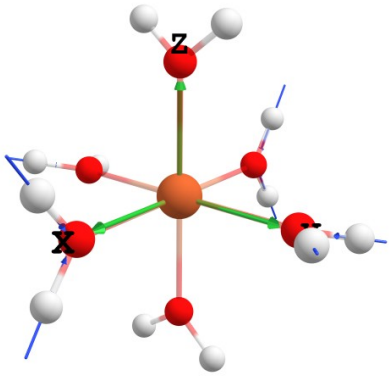
46	3719.68	Ligand Based	-	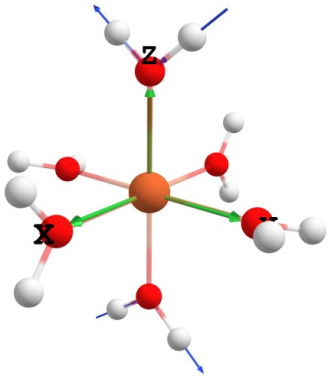
47	3720.59	Ligand Based	-	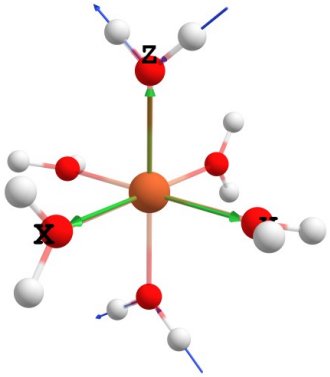

48	3728.26	Ligand Based	-	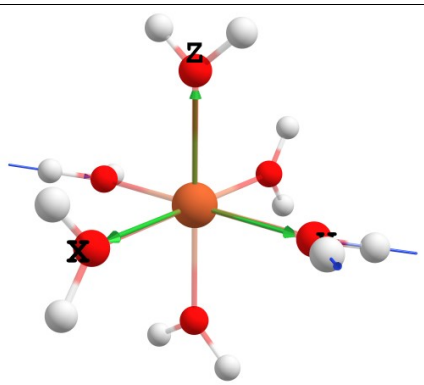
49	3728.97	Ligand Based	-	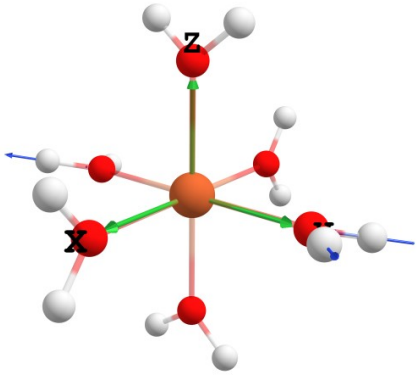
50	3733.33	Ligand Based	-	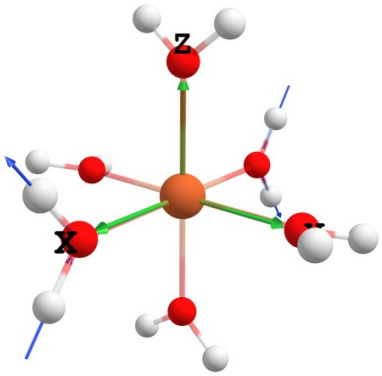
51	3733.77	Ligand Based	-	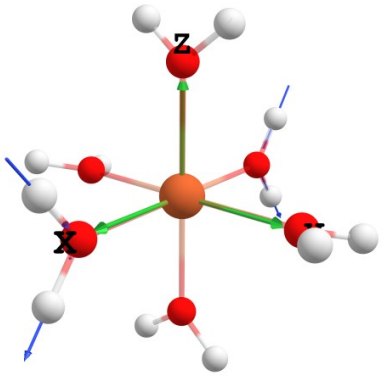

Table S4. Spin-phonon coupling fits for the neutron diffraction structure of $[Fe(H_2O)_6]^{2+}$ including linear and quadratic fits vs. Q_i. Note only ligand–metal-based modes are included here.[a]

Mode	Energy/ cm^{-1}	Symm.	Linear			Quadratic			
			m	b	r^2	a	b	c	r^2
19	54.2	-	0.0005	9.6478	0.2354	-0.1669	0.0005	9.6478	0.9991
20	117.4	-	0.0009	9.6479	0.0005	-3.6605	0.0009	9.6481	0.2829
21	117.44	-	0	9.648	0	5.4035	0	9.6478	0.9579
22	134.82	t_{2g}	0.0016	9.6474	0.0022	-4.6219	0.0016	9.6476	0.6467
23	134.83	t_{2g}	-0.0251	9.6475	0.3251	-4.5302	-0.0251	9.6477	0.6794
24	170.38	-	0.0007	9.6476	0.0016	-1.5865	0.0007	9.6477	0.2701
25	170.43	-	0.0017	9.6478	0.0315	-1.0044	0.0017	9.6479	0.4025
26	**181.11**	$\boldsymbol{t_{2g}}$	**-1.1179**	**9.648**	**0.9997**	3.1884	-1.1179	9.6478	1
27	217.05	-	-0.0006	9.6479	0.0015	2.5998	-0.0006	9.6478	0.9999
28	244.13	$e_g(\varepsilon)$	-0.0013	9.6471	0.0003	-12.3896	-0.0013	9.6476	0.8611
29	244.16	$e_g(\theta)$	-0.0517	9.6473	0.4285	-9.4148	-0.0517	9.6477	0.9035
30	333.54	t_{2u}	0.0103	9.6475	0.0845	-5.791	0.0103	9.6477	0.9695
31	333.57	t_{2u}	-0.0003	9.6478	0.0001	-2.6367	-0.0003	9.6479	0.2667
32	**340.62**	$\boldsymbol{a_{1g}}$	**-4.431**	**9.6479**	**1**	1.8106	-4.431	9.6478	1
33	341.42	t_{2u}	-0.0608	9.6477	0.9249	-2.9987	-0.0608	9.6478	1

[a]Shaded boxes indicate entries where a quadratic fit was better than a linear fit. Modes discussed in the manuscript text are bolded.

Table S5. Spin-phonon coupling fits for BP86 optimized $[Fe(H_2O)_6]^{2+}$ including linear and quadratic fits vs Q_i. Note there is a gap in energy from mode 33 to 34 (the next mode being at ~1600 cm^{-1}). Thus, only modes up to 33 are included here.[a]

Mode	Energy/ cm^{-1}	Symm.	Linear			Quadratic			
			m	b	r^2	a	b	c	r^2
1	63.88	t_{2g}	-0.2965	18.2752	0.9260	-13.7911	-0.2965	18.2758	0.9929
2	72.99	-	0.0000	18.2758	0.0000	-5.5089	0.0000	18.2760	1.0000
3	79.01	-	0.0000	18.2763	0.0000	5.2119	0.0000	18.2760	0.9998
4	80.85	t_{2g}	0.7113	18.2740	0.8821	-43.4159	0.7113	18.2759	0.9919
5	85.79	-	0.0000	18.2760	0.0000	-1.8606	0.0000	18.2760	0.9999
6	94.01	-	0.6756	18.2737	0.8881	-36.1517	0.6756	18.2753	0.9730
7	**105.6**	$\boldsymbol{t_{2g}}$	**-3.9211**	**18.2763**	**0.9999**	5.6769	-3.9211	18.2761	1.0000
8	106.24	-	0.0002	18.2760	0.0391	0.2107	0.0002	18.2760	0.9936
9	129.13	-	0.0001	18.2760	0.0082	0.1016	0.0001	18.2760	0.9899
10	138.63	-	0.0000	18.2760	0.0000	-1.1844	0.0000	18.2760	1.0000
11	**170.62**	$\boldsymbol{e_g\,(\varepsilon)}$	**-21.2392**	**18.2688**	**0.9973**	-51.1583	-21.2392	18.2710	0.9975
12	179.06	-	-0.0002	18.2758	0.0000	-6.3136	-0.0002	18.2760	1.0000
13	**227.31**	$\boldsymbol{e_g\,(\theta)}$	**5.8232**	**18.2728**	**0.9946**	-71.2899	5.8232	18.2760	0.9995
14	234.35	-	0.0000	18.2763	0.0000	5.1013	0.0000	18.2760	1.0000
15	260.87	-	0.0647	18.2759	0.7266	-3.8828	0.0647	18.2761	0.8138
16	273	-	0.0025	18.2762	0.0309	2.4386	0.0025	18.2760	0.9995
17	273.82	-	-26.8343	18.2779	0.9999	42.4525	-26.8343	18.2760	1.0000
18	295.53	t_{1u}	0.0000	18.2763	0.0000	5.5721	0.0000	18.2760	1.0000
19	299.86	t_{1u}	0.0001	18.2757	0.0000	-7.3042	0.0001	18.2760	1.0000
20	309.74	-	0.6806	18.2749	0.9589	-21.1585	0.6806	18.2759	0.9899
21	**323.31**	$\boldsymbol{a_{1g}}$	**11.7991**	**18.2753**	**0.9999**	-16.5058	11.7991	18.2761	1.0000
22	334.85	-	0.6654	18.2741	0.7922	-48.5051	0.6654	18.2763	0.9327
23	336.61	t_{1u}	-0.0001	18.2764	0.0000	8.7799	-0.0001	18.2760	1.0000
24	346.38	-	7.8526	18.2750	0.9996	-24.9370	7.8526	18.2761	1.0000
25	347.46	-	-0.0004	18.2759	0.0010	-2.1965	-0.0004	18.2760	1.0000
26	372.31	-	0.0000	18.2765	0.0000	9.2376	0.0000	18.2760	1.0000
27	404.75	-	0.0000	18.2764	0.0000	8.8995	0.0000	18.2760	1.0000
28	482.99	-	0.9769	18.2741	0.8936	-49.8298	0.9769	18.2763	0.9712
29	503.06	-	18.7352	18.2763	1.0000	5.9751	18.7352	18.2761	1.0000
30	505.64	-	-0.0001	18.2761	0.0007	0.9607	-0.0001	18.2760	0.9996
31	511.04	-	-0.9525	18.2748	0.9753	-23.3168	-0.9525	18.2758	0.9948
32	529.33	-	0.0000	18.2760	0.0000	-0.8538	0.0000	18.2760	0.9998
33	535.82	-	0.0000	18.2763	0.0000	5.7882	0.0000	18.2760	1.0000

[a]Shaded boxes indicate entries where a quadratic fit was better than the linear fit. Modes discussed in the manuscript text are bolded. While mode 17 exhibits an appreciable slope, it is a mode that is mostly water rotation-based and is thus not ligand–metal based and is not considered further here.

Table S6. Spin-phonon coupling fits for the hydrogen optimized structure based on X-ray crystallographic structures of $[Fe(NH_3)_6]^{2+}$, including linear and quadratic fits vs Q_i.[a]

Mode	Energy / cm^{-1}	Symm.	Linear			Quadratic			
			m	b	r^2	a	b	c	r^2
1	-27.07	-	-1.7434	37.9213	1.0000	0.5179	-1.7434	37.9213	1.0000
2	51.7	-	-0.3977	37.9210	0.9927	-5.8971	-0.3977	37.9213	1.0000
3	55.9	-	-1.0249	37.9212	1.0000	-1.1650	-1.0249	37.9213	1.0000
4	77.58	-	4.3730	37.9212	1.0000	-1.7549	4.3730	37.9213	1.0000
5	82.76	-	-7.8728	37.9209	1.0000	-8.0381	-7.8728	37.9213	1.0000
6	101.28	-	-0.9521	37.9213	1.0000	-0.2290	-0.9521	37.9213	1.0000
7	107	-	-8.2866	37.9212	1.0000	-2.1854	-8.2866	37.9213	1.0000
8	108.65	-	-5.4703	37.9211	1.0000	-4.3460	-5.4703	37.9213	1.0000
9	119.15	-	2.1759	37.9213	1.0000	-0.6089	2.1759	37.9213	1.0000
10	139.95	-	-0.7126	37.9204	0.9767	-19.0634	-0.7126	37.9213	1.0000
11	152.57	-	-2.5939	37.9213	1.0000	-0.1717	-2.5939	37.9213	1.0000
12	153.87	-	-2.1634	37.9215	0.9998	4.7109	-2.1634	37.9213	1.0000
13	157.27	t_{2g}	-2.2044	37.9206	0.9986	-14.4823	-2.2044	37.9213	1.0000
14	159.05	t_{2g}	2.8408	37.9201	0.9970	-26.7532	2.8408	37.9213	0.9999
15	**167.6**	$\boldsymbol{t_{2g}}$	**-13.6336**	**37.9216**	**1.0000**	6.0703	-13.6336	37.9213	1.0000
16	235.45	$e_g\,(\varepsilon)$	-2.1271	37.9075	0.6176	-289.4976	-2.1271	37.9204	0.9994
17	**242.83**	$\boldsymbol{e_g\,(\theta)}$	**-37.3585**	**37.9221**	**1.0000**	10.9126	-37.3585	37.9216	1.0000
18	307.49	t_{1u}	2.6162	37.9202	0.9972	-23.5627	2.6162	37.9213	0.9999
19	313.98	t_{1u}	-5.4174	37.9196	0.9986	-34.1913	-5.4174	37.9211	1.0000
20	**314.5**	$\boldsymbol{t_{1u}}$	**-14.6084**	**37.9208**	**1.0000**	-10.3869	-14.6084	37.9213	1.0000
21	**340.93**	$\boldsymbol{a_{1g}}$	**-8.7440**	**37.9211**	**1.0000**	-4.3820	-8.7440	37.9213	1.0000
22	417.86	-	4.4640	37.9209	0.9999	-9.2027	4.4640	37.9213	1.0000
23	421.63	-	-1.3120	37.9209	0.9987	-8.0804	-1.3120	37.9213	1.0000
24	435.83	-	-2.4432	37.9216	0.9998	6.0430	-2.4432	37.9213	1.0000
25	466.72	-	11.9067	37.9194	0.9996	-42.2238	11.9067	37.9213	1.0000
26	479	-	9.2553	37.9201	0.9997	-25.7504	9.2553	37.9213	1.0000
27	495.83	-	17.4463	37.9219	1.0000	12.7757	17.4463	37.9213	1.0000
28	552.19	-	3.7600	37.9047	0.7526	-373.0824	3.7600	37.9213	1.0000
29	567.7	-	24.5778	37.9196	0.9999	-37.9132	24.5778	37.9213	1.0000
30	571.89	-	0.4614	37.9185	0.6341	-58.9619	0.4614	37.9211	0.9797
31	579.07	-	-55.8946	37.9235	1.0000	48.9961	-55.8946	37.9213	1.0000
32	580.72	-	60.5911	37.9243	1.0000	66.5179	60.5911	37.9213	1.0000
33	583.41	-	-2.8825	37.9206	0.9989	-16.5241	-2.8825	37.9213	1.0000

[a]Shaded boxes indicate entries where a quadratic fit was better than the linear fit. Modes discussed in the manuscript text are bolded. Note the small imaginary mode is a concerted NH_3 rotation.

Table S7. Spin-phonon coupling fits for BP86 optimized $[Fe(NH_3)_6]^{2+}$, including linear and quadratic fits vs Q_i.[a]

Mode	Energy / cm^{-1}	Symm.	Linear			Quadratic			
			m	b	r^2	a	b	c	r^2
1	5.23	-	-1.2808	38.4412	1.0000	0.9791	-1.2808	38.4411	1.0000
2	52.92	-	-1.8335	38.4410	0.9999	-2.1155	-1.8335	38.4411	1.0000
3	58.14	-	0.7303	38.4410	0.9995	-2.7182	0.7303	38.4411	1.0000
4	73.28	-	1.7488	38.4407	0.9990	-9.4886	1.7488	38.4411	1.0000
5	83.62	-	8.0131	38.4414	0.9998	-3.2021	8.0131	38.4415	0.9998
6	98.96	-	0.7636	38.4411	0.9999	0.2713	0.7636	38.4411	1.0000
7	105.95	-	7.9593	38.4393	0.9992	-39.6432	7.9593	38.4410	1.0000
8	107.49	-	0.5945	38.4410	0.9969	-1.3249	0.5945	38.4411	0.9971
9	114.04	-	-0.7336	38.4408	0.9968	-7.1054	-0.7336	38.4412	0.9999
10	143.09	t_{2g}	2.2823	38.4402	0.9983	-6.1131	2.2823	38.4405	0.9986
11	147.44	-	1.0898	38.4399	0.9791	-27.5286	1.0898	38.4411	1.0000
12	149.29	t_{2g}	1.8144	38.4369	0.9260	-88.4080	1.8144	38.4408	0.9994
13	152.31	-	-2.7083	38.4412	1.0000	0.8115	-2.7083	38.4412	1.0000
14	153.14	-	0.3148	38.4401	0.9260	-13.9715	0.3148	38.4407	0.9868
15	**159.08**	$\boldsymbol{t_{2g}}$	**-13.1283**	**38.4410**	**1.0000**	2.0732	-13.1283	38.4409	1.0000
16	186.24	$e_g\,(\varepsilon)$	-1.0652	38.4271	0.2711	-300.8520	-1.0652	38.4405	0.9930
17	**190.84**	$\boldsymbol{e_g\,(\theta)}$	**-41.5507**	**38.4396**	**1.0000**	-25.3664	-41.5507	38.4407	1.0000
18	249.63	t_{1u}	-0.3751	38.4401	0.9624	-9.5143	-0.3751	38.4405	0.9831
19	256.15	t_{1u}	1.7536	38.4389	0.9797	-43.2987	1.7536	38.4408	0.9996
20	**264.89**	$\boldsymbol{t_{1u}}$	**-14.2432**	**38.4402**	**0.9999**	-19.7061	-14.2432	38.4411	1.0000
21	**294.77**	$\boldsymbol{a_{1g}}$	**9.5663**	**38.4395**	**0.9995**	-36.8403	9.5663	38.4412	1.0000
22	417.04	-	-0.8112	38.4399	0.9852	-15.2415	-0.8112	38.4406	0.9969
23	418.99	-	1.7483	38.4402	0.9967	-14.5814	1.7483	38.4409	0.9990
24	429.12	-	-1.1207	38.4412	0.9996	-0.0200	-1.1207	38.4412	0.9996
25	465.05	-	-7.8877	38.4408	0.9996	3.1573	-7.8877	38.4406	0.9996
26	473.37	-	-4.2434	38.4391	0.9978	-33.9318	-4.2434	38.4406	0.9999
27	490.2	-	14.9930	38.4418	0.9999	6.2981	14.9930	38.4415	0.9999
28	543.76	-	-1.2314	38.4264	0.3071	-319.7494	-1.2314	38.4406	0.9982
29	559.58	-	13.5791	38.4398	0.9998	-24.5792	13.5791	38.4409	0.9999
30	561.92	-	-5.4727	38.4324	0.9497	-207.6423	-5.4727	38.4417	0.9954
31	568.09	-	-7.2615	38.4384	0.9978	-57.4980	-7.2615	38.4409	0.9999
32	574.05	-	-77.8267	38.4452	0.9999	98.8017	-77.8267	38.4408	1.0000
33	575.64	-	5.6653	38.4388	0.9979	-42.0788	5.6653	38.4407	0.9997

[a]Shaded boxes indicate entries where a quadratic fit was better than the linear fit. Modes discussed in the manuscript text are bolded.

Table S8. Linear excited state coupling term slopes for the neutron diffraction structure of $[Fe(H_2O)_6]^{2+}$ vs Q_i.

Mode #	Slope D	Slope Δ	Slope E_g(1a)	Slope E_g(1b)
19	0.00053537	0	0	0
20	0.00092631	-2.6640134	-4.2688407	-1.059186
21	-4.654E-05	-0.529593	0	-1.059186
22	0.0015708	-3.2257029	-16.08037	9.62896392
23	-0.0250729	5.87366799	16.0482732	-4.3009372
24	0.00071768	1.74E-16	0	0
25	0.00169149	0	0	1.74E-16
26	**-1.1178665**	**1425.58416**	**1425.05456**	**1426.11375**
27	-0.0005787	0	3.4799E-16	0
28	-0.0012675	0.54564129	78.3797663	-77.288484
29	-0.0516639	12.3090255	71.8320709	-47.21402
30	0.01033958	-3.7552959	-5.3601233	-2.1504686
31	-0.0003216	-1.6208756	-1.0912826	-2.1504686
32	**-4.4309924**	**1457.16716**	**1455.03274**	**1459.30158**
33	-0.0608249	19.2739761	18.1987418	20.3492104

Table S9. Linear excited state coupling term slopes for BP86 optimized $[Fe(H_2O)_6]^{2+}$ vs Q_i.

Mode	Slope D	Slope Δ	Slope E_g(1a)	Slope E_g(1b)
1	-0.2965432	4.28488895	14.9890872	-6.4193093
2	3.2097E-05	6.3299E-28	0	-6.33E-28
3	-3.21E-05	6.3299E-28	0	-6.33E-28
4	0.71126107	-10.704198	-41.757607	20.3492104
5	-1.027E-05	6.3299E-28	0	-6.33E-28
6	0.67560823	-5.8897163	-26.76852	14.9890872
7	**-3.9210637**	**324.945436**	**209.84722**	**440.043651**
8	0.0002465	6.3299E-28	0	-6.33E-28
9	5.3601E-05	6.3299E-28	0	-6.33E-28
10	3.2097E-05	6.3299E-28	0	-6.33E-28
11	**-21.239228**	**468.882398**	**671.170882**	**266.593914**
12	-0.0001608	0	0	-6.33E-28
13	**5.82318237**	**65.846065**	**-1179.869**	**1311.56118**
14	4.3009E-05	6.3299E-28	0	-6.33E-28
15	0.06474965	-1.6048273	-18.198742	14.9890872
16	0.00251605	6.3299E-28	0	-6.33E-28
17	-26.834335	1090.48016	950.763898	1230.19643
18	-2.15E-05	6.3299E-28	0	-6.33E-28
19	9.629E-05	0	0	-6.33E-28
20	0.68061561	-19.803569	-29.978174	-9.6289639
21	**11.7991234**	**-404.70535**	**-500**	**-309.41071**
22	0.66544133	-11.24984	-58.897163	36.3974836
23	-6.419E-05	6.3299E-28	0	-6.33E-28
24	7.85261972	-193.25331	-296.57209	-89.934523
25	-0.0003961	6.3299E-28	0	-6.33E-28
26	-2.118E-05	6.3299E-28	0	-6.33E-28
27	0	6.3299E-28	0	-6.33E-28
28	0.97688856	-29.448581	-28.918988	-29.978174
29	18.7351602	-932.01951	-663.82077	-1200.2183
30	-0.0001499	6.3299E-28	0	-6.33E-28
31	-0.9524522	49.7817435	54.5962254	44.9672615
32	7.64E-14	6.3299E-28	0	-6.33E-28
33	-4.301E-05	6.3299E-28	0	-6.33E-28

Table S10. Linear excited state coupling term slopes for hydrogen optimized X-ray crystal structure of $[Fe(NH_3)_6]^{2+}$ vs Q_i.

Mode	Slope D	Slope Δ	Slope E_g(1a)	Slope E_g(1b)
1	-1.7434472	23.5588651	23.5588651	23.5588651
2	-0.3977301	5.36012325	-12.838619	23.5588651
3	-1.0249345	18.1987418	-6.4193093	42.8167929
4	4.3729975	-64.241238	-36.397484	-92.084992
5	-7.8728373	115.627808	104.92361	126.332007
6	-0.9520766	11.7794325	17.1395558	6.41930928
7	-8.2866485	116.703043	96.3538323	137.052253
8	-5.4702789	83.5152138	53.5370394	113.493388
9	2.175943	-29.448581	-35.338298	-23.558865
10	-0.7126207	24.6180511	-50.327385	99.563487
11	-2.5939084	29.9781743	66.375658	-6.4193093
12	-2.1634045	26.7685197	36.3974836	17.1395558
13	-2.2043683	31.5830017	-20.34921	83.5152138
14	2.84080723	-42.2872	-9.6289639	-74.945436
15	-13.633634	206.637566	107.074079	306.201053
16	-2.1270863	29.4485813	56.7466941	2.15046861
17	-37.358511	401.495699	826.550263	-23.558865
18	2.61616671	-44.967262	-6.4193093	-83.515214
19	-5.4174287	67.4508923	63.1660033	71.7357812
20	-14.608392	199.143022	164.879959	233.406086
21	-8.7439556	101.713956	96.3538323	107.074079
22	4.46397291	-53.537039	-83.515214	-23.558865
23	-1.3120343	16.5939145	23.5588651	9.62896392
24	-2.4431692	41.7576069	23.5588651	59.9563487
25	11.9067435	-195.93337	-59.956349	-331.91039
26	9.25533413	-126.87765	-143.47156	-110.28373
27	17.4463471	-200.21826	-390.80755	-9.6289639
28	3.76000931	-77.079856	-104.92361	-49.236102
29	24.5777963	-334.04481	-388.65708	-279.43253
30	0.46137116	-17.669149	89.934523	-125.27282
31	-55.894571	809.956349	589.934523	1029.97817
32	60.5911205	-873.12235	-616.70304	-1129.5417
33	-2.8825215	40.6823726	-5.3601233	86.7248684

Table S11. Linear excited state coupling term slopes for BP86 optimized $[Fe(NH_3)_6]^{2+}$ vs Q_i.

Mode	Slope D	Slope Δ	Slope E_g(1a)	Slope E_g(1b)
1	-1.2808236	16.0643215	17.1395558	14.9890872
2	-1.8334972	25.6932854	9.62896392	41.7576069
3	0.73031005	-5.8897163	-17.139556	5.36012325
4	1.74883008	-25.693285	-12.838619	-38.547952
5	8.01311433	-118.30787	-96.353832	-140.26191
6	0.76364745	-10.704198	-11.779433	-9.6289639
7	7.95926371	-109.73809	-99.563487	-119.9127
8	0.59453364	-16.593914	6.41930928	-39.607138
9	-0.7335897	10.7041982	6.41930928	14.9890872
10	2.28225286	-41.757607	9.62896392	-93.144178
11	1.08984979	-22.483631	44.9672615	-89.934523
12	1.81443992	-27.298113	23.5588651	-78.155091
13	-2.7083281	32.658236	20.3492104	44.9672615
14	0.31484915	-4.2848889	18.1987418	-26.76852
15	-13.128321	207.7128	66.375658	349.049942
16	-1.0651996	10.7041982	14.9890872	6.41930928
17	-41.550744	451.823084	870.458339	33.187829
18	-0.3751162	7.49454359	-9.6289639	24.6180511
19	1.75356625	-28.373347	6.41930928	-63.166003
20	-14.243178	187.36359	186.288355	188.438824
21	9.56634613	-114.02298	-123.12235	-104.92361
22	-0.8112052	10.7041982	29.9781743	-8.5697779
23	1.74831301	-24.088458	-36.397484	-11.779433
24	-1.1207055	20.8788034	6.41930928	35.3382976
25	-7.8877202	133.296957	20.3492104	246.244704
26	-4.2433502	57.2762871	66.375658	48.1769162
27	14.9929885	-170.24008	-320.13095	-20.34921
28	-1.2314065	45.4968545	51.3865708	39.6071383
29	13.5791013	-174.52497	-244.12633	-104.92361
30	-5.4727282	78.1550905	-41.757607	198.067788
31	-7.2614719	106.528438	114.552574	98.5043009
32	-77.826721	1117.23264	769.803569	1464.6617
33	5.66534761	-76.550263	0	-153.10053

Table S12. Linear spin–phonon coupling term slopes for BP86 optimized $[Fe(H_2O)_6]^{2+}$ with various numbers of states and different active spaces vs Q_i.

	Linear slope of D vs Q_i					
	6 elections, 5 orbitals				**10 electrons, 7 orbitals**	
Mode	**3, 0, 0**	**5, 0, 0**	**5, 17, 15**	**5, 45, 50**	**5, 17, 15**	**5, 45, 50**
1	-0.2273	-0.2794	-0.2965	-0.2576	-0.5871	-0.2532
2	0	0	0	0.0001	0	-0.0448
3	0	0	0	0	0	0.0894
4	0.7777	1.0164	0.7113	0.6274	1.7114	1.3292
5	0	0	0	0	0	-0.0544
6	0.2846	0.4515	0.6756	0.4979	1.5295	1.1722
7	**-6.058**	**-4.8411**	**-3.9211**	**-3.84**	**-4.5804**	**-3.3889**
8	0.0004	0.0003	0.0002	0.0003	0.0002	0.0734
9	0	0	0.0001	0.0001	0.0001	-0.0132
10	0	0	0	0.0001	0	-0.1206
11	**-14.7181**	**-19.1021**	**-21.2392**	**-22.3501**	**-21.5445**	**-22.7663**
12	-0.0002	-0.0002	-0.0002	-0.0001	-0.0002	-0.0137
13	**4.5268**	**5.1848**	**5.8232**	**6.1238**	**5.4454**	**5.7397**
14	0.0001	0.0001	0	0.0001	0.0001	0.0824
15	-0.0668	-0.2	0.0647	0.0575	-0.4353	-0.4704
16	0.0028	0.0028	0.0025	0.0027	0.0024	0.0229
17	-30.4986	-29.7585	-26.8343	-28.5514	-25.071	-28.34
18	0	0.0001	0	0	0.0001	0.0939
19	0.0001	0.0001	0.0001	0.0001	0.0001	-0.0287
20	0.7616	1.0264	0.6806	0.6038	1.4691	1.3449
21	**13.1456**	**12.8872**	**11.7991**	**12.5705**	**12.2066**	**13.0277**
22	0.9487	1.0055	0.6654	0.5439	1.5153	0.7756
23	-0.0001	-0.0001	-0.0001	-0.0001	-0.0001	-0.0395
24	7.6501	8.3662	7.8526	8.4027	7.7935	8.0108
25	-0.0004	-0.0005	-0.0004	-0.0004	-0.0004	0.2084
26	-	-	0	0	0	0.6315
27	-	-	0	0	0.0001	0.5189
28	-	-	0.9769	0.992	2.0506	1.5055
29	-	-	18.7352	19.2623	18.6694	19.1651
30	-	-	-0.0001	-0.0001	-0.0001	-0.0387
31	-	-	-0.9525	-0.9251	-1.5222	-1.1066
32	-	-	0	0	0	-0.0401
33	-	-	0	0	0	-0.0794

Note that linear spin–phonon coupling terms are similar between the 6, 5, or 10, 7 active spaces with either 5 quintets, 17 triplets, and 15 singlets or 5 quintets, 45 triplets, and 50 singlets.

C. Figures

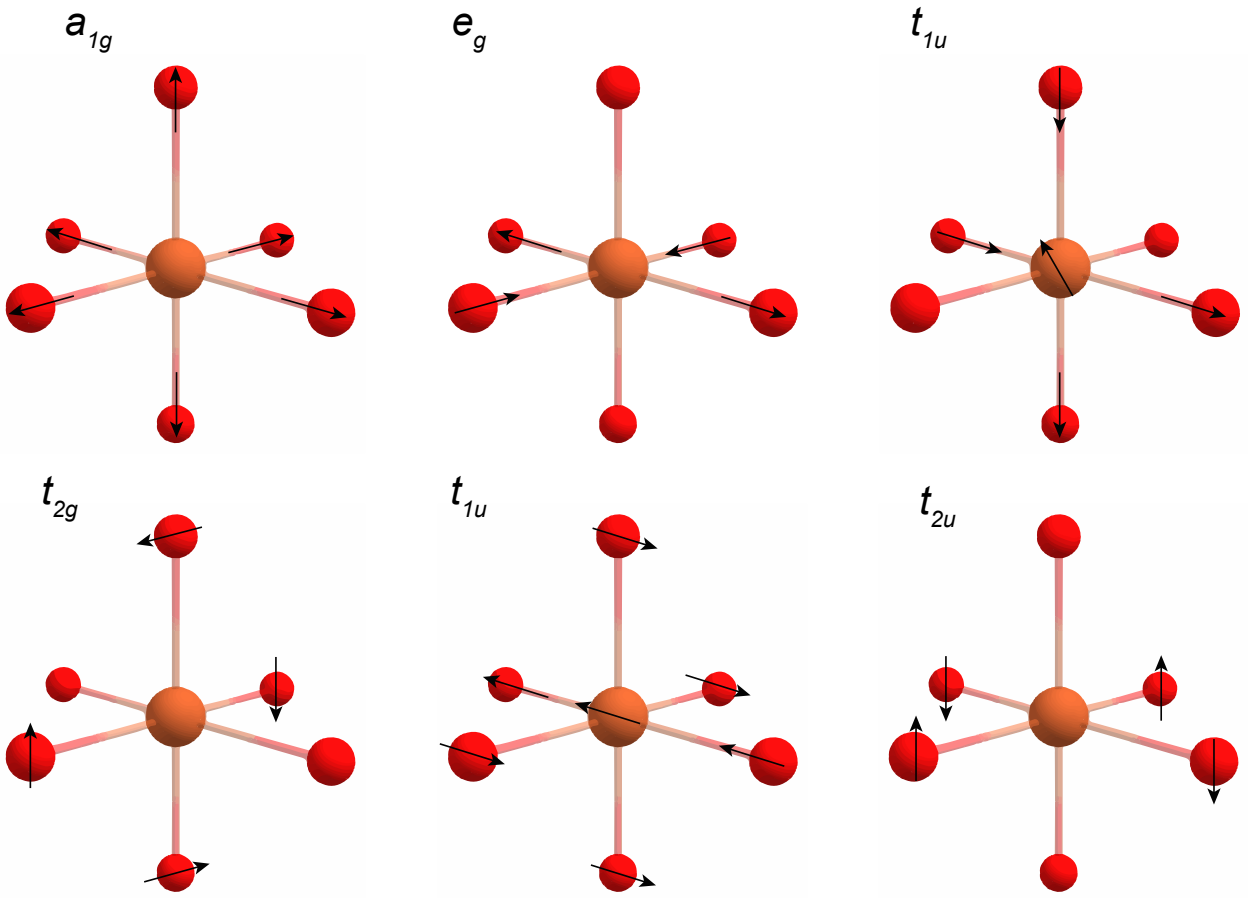

Figure S1. Specific components of the 15 octahedral normal modes of vibration.

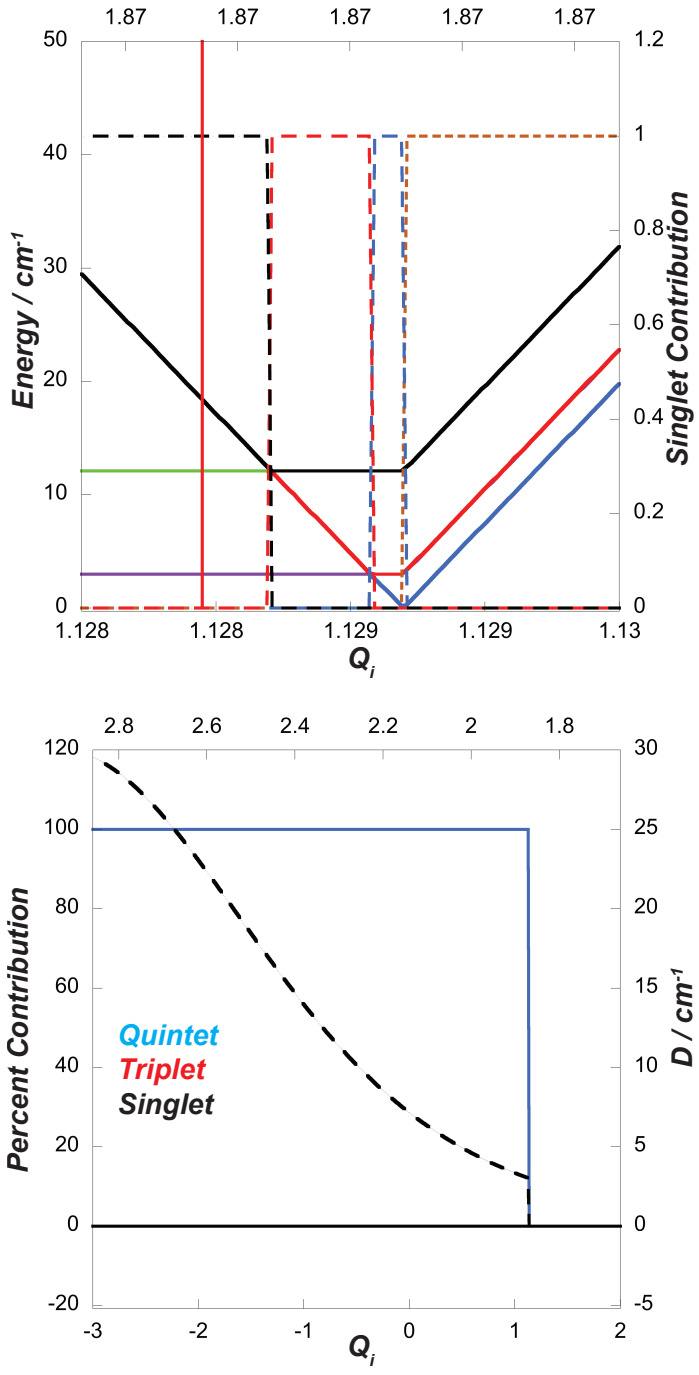

Figure S2. Intersystem crossing in the neutron diffraction structure of $[Fe(H_2O)_6]^{2+}$ with 5 quintets, 0 triplets, 15 singlets. No interactions/mixings between the S = 0 $^1A_{1g}$ excited state and the S=2 M_s sublevels of the ground state are observed (top panel). Furthermore, only the quintet states contribute to the overall ZFS (bottom panel).

D. Structures and Input Coordinates

Cartesian Coordinates / Å

$[Fe(H_2O)_6]^{2+}$ neutron diffraction structure

Fe	0.000000	0.000000	0.000000
O	2.139489	0.000000	0.050626
O	0.000032	-0.000132	-2.140099
O	-0.049399	2.138917	-0.050633
O	-2.139513	-0.000060	-0.050549
O	0.000000	0.000000	2.140136
O	0.049454	-2.138989	0.050593
H	2.701326	0.408707	-0.547140
H	2.564031	-0.519150	0.583604
H	-0.531080	0.510584	-2.577062
H	0.422792	-0.601296	-2.687642
H	-0.569769	2.551341	-0.591941
H	0.538781	2.710012	0.359064
H	-2.564055	0.519092	-0.583528
H	-2.701374	-0.408872	0.547126
H	0.531056	-0.510644	2.577138
H	-0.422816	0.601237	2.687718
H	0.569689	-2.551374	0.591890
H	-0.538805	-2.710118	-0.359155

$[Fe(H_2O)_6]^{2+}$ BP86 optimized structure

Fe	0.000000	0.000000	0.000000
O	2.161054	0.000000	-0.024716
O	-0.000001	0.000001	-2.127560
O	-0.004763	2.165914	0.006737
O	-2.161054	0.000001	0.024717
O	0.000000	0.000000	2.127560
O	0.004765	-2.165914	-0.006739
H	2.744550	0.005829	-0.805953
H	2.736964	0.004339	0.762222
H	0.058401	0.784861	-2.704620
H	0.063376	-0.785197	-2.703626
H	-0.760535	2.744241	-0.206710
H	0.746496	2.751294	0.216701
H	-2.736964	-0.004337	-0.762222
H	-2.744549	-0.005831	0.805954
H	-0.058400	-0.784860	2.704620
H	-0.063377	0.785198	2.703626
H	0.760537	-2.744240	0.206709
H	-0.746494	-2.751294	-0.216704

$[Fe(NH_3)_6]^{2+}$ hydrogen optimized X-ray crystallographic based structure

Fe	0.000047	-0.000760	0.000511
N	0.003198	0.001512	2.223008
H	-0.146409	0.933391	2.628352
H	0.866714	-0.334721	2.666948
H	-0.737379	-0.576490	2.639399
N	-0.079425	-0.096827	-2.218481
H	-0.390873	0.763554	-2.686289
H	-0.733023	-0.813988	-2.555811
H	0.811183	-0.325491	-2.676668
N	-2.220209	0.098294	0.012658
H	-2.600033	0.651441	-0.765555
H	-2.702555	-0.805044	-0.072112
H	-2.633593	0.528272	0.849448
N	2.221448	-0.003774	-0.069236
H	2.598942	0.607000	-0.804200
H	2.686624	0.325306	0.785863
H	2.655057	-0.915871	-0.258995
N	0.086153	2.218030	-0.096179
H	-0.822225	2.695904	-0.141240
H	0.614540	2.601804	-0.889659
H	0.547182	2.623762	0.727235
N	-0.012321	-2.219720	0.124397
H	0.718313	-2.610785	0.732054
H	0.147281	-2.670276	-0.784763
H	-0.881436	-2.644727	0.470518

$[Fe(NH_3)_6]^{2+}$ BP86 Optimized Structure

Fe	0.008702	0.004958	-0.009045
N	-0.002320	0.050468	2.295970
H	-0.228489	0.963481	2.707232
H	0.884683	-0.222288	2.734929
H	-0.693712	-0.591600	2.700677
N	-0.051183	-0.132883	-2.308472
H	-0.192342	0.761651	-2.791963
H	-0.816853	-0.727260	-2.646912
H	0.793028	-0.530790	-2.736133
N	-2.282648	0.062804	-0.031407
H	-2.643054	0.782018	-0.668991
H	-2.734732	-0.805464	-0.341149
H	-2.714013	0.273379	0.875896
N	2.285633	0.033166	-0.078332
H	2.664571	0.619168	-0.831515
H	2.743402	0.375231	0.774576
H	2.692476	-0.895077	-0.241272
N	0.110380	2.283035	-0.057009
H	-0.799225	2.721812	0.126635
H	0.423259	2.689528	-0.946335
H	0.740130	2.683487	0.648216
N	-0.048502	-2.278969	0.126662
H	0.757748	-2.651969	0.640937
H	-0.033569	-2.765935	-0.776837
H	-0.865180	-2.661391	0.617554

$[Co(NH_3)_6]^{3+}$ BP86 Optimized Structure

Co	0.004573	-0.057465	-0.056375
N	2.208682	-0.100900	-0.247027
N	-0.078423	0.300244	-2.217471
N	0.011593	-2.240557	0.132216
H	2.690395	-0.370250	0.622902
H	2.552099	-0.760388	-0.960215
H	0.018261	-0.583491	-2.741843
H	-0.960378	0.716636	-2.549396
H	0.669574	0.910939	-2.576592
H	-0.731778	-2.618807	0.737191
H	-0.131474	-2.690230	-0.785888
H	0.891224	-2.637700	0.493249
H	2.621888	0.807346	-0.503556
N	-2.208492	-0.160160	-0.029313
H	-2.597464	-0.468017	0.873684
H	-2.603647	-0.809446	-0.725025
H	-2.665449	0.744177	-0.215751
N	-0.075627	2.163737	0.188565
N	0.167216	0.009986	2.172344
H	-0.723660	2.463561	0.930100
H	-0.382774	2.666736	-0.656094
H	0.832422	2.582427	0.434953
H	0.446692	-0.884269	2.600419
H	-0.713053	0.267616	2.640868
H	0.861321	0.694404	2.503975

E. Representative ORCA Input Files

Representative ORCA input file for a geometry optimization

```
! UKS BP86 def2-TZVP def2/J Opt  RI TIGHTSCF Grid7 NoFinalGrid GridX9 NoFinalGridX
! SlowConv PrintBasis normalprint
%scf
        MaxIter 1000
        Shift Shift 0.5 ErrOff 0.1 end
end
%pal
        nprocs 8
end
%maxcore 9000
* xyzfile 2 5 structure.xyz
```

Representative ORCA input file for a frequency calculation

```
! UKS BP86 def2-TZVP def2/J Freq RI TIGHTSCF Grid7 NoFinalGrid GridX9 NoFinalGridX
! SlowConv PrintBasis normalprint
%scf
        MaxIter 1000
        Shift Shift 0.5 ErrOff 0.1 end
end
%pal
        nprocs 8
end
%maxcore 9000
* xyzfile 2 5 structure.xyz
```

Representative ORCA input file for CASSCF/NEVPT2 calculation

```
! PATOM def2-TZVP def2-TZVP/C XYZfile largeprint
%casscf
        nel 6
        norb 5
        mult 5,3,1
        nroots 5,17,15
        trafostep RI
        nevpt2 SC
        rel
                printlevel 3
                dosoc true
                 mcd true
                NInitStates 5
                NPointsTheta 10
                 NPointsPsi 10
                 NPointsPhi 10
                B 5000
                Temperature 10
                gtensor true
                dtensor true
         end
end
%pal
        nprocs 1
end
%maxcore 9000
* xyzfile 2 5 structure.xyz
```

References

[1] F. Neese, WIREs Computational Molecular Science **2**, 73 (2012).
[2] F. Neese, WIREs Computational Molecular Science **8**, e1327 (2018).
[3] J.P. Perdew, Physical Review B **33**, 8822 (1986).
[4] A.D. Becke, Physical Review A **38**, 3098 (1988).
[5] A.D. Becke, The Journal of Chemical Physics **98**, 5648 (1993).
[6] F. Weigend, F. Furche, and R. Ahlrichs, The Journal of Chemical Physics **119**, 12753 (2003).
[7] C. Angeli, R. Cimiraglia, and J.-P. Malrieu, Chemical Physics Letters **350**, 297 (2001).
[8] C. Angeli, R. Cimiraglia, S. Evangelisti, T. Leininger, and J.-P. Malrieu, The Journal of Chemical Physics **114**, 10252 (2001).
[9] C. Angeli, R. Cimiraglia, and J.-P. Malrieu, The Journal of Chemical Physics **117**, 9138 (2002).
[10] R.W.A. Havenith, P.R. Taylor, C. Angeli, R. Cimiraglia, and K. Ruud, The Journal of Chemical Physics **120**, 4619 (2004).
[11] I. Schapiro, K. Sivalingam, and F. Neese, Journal of Chemical Theory and Computation **9**, 3567 (2013).